



Lawrence Berkeley Laboratory

UNIVERSITY OF CALIFORNIA

Materials & Molecular Research Division

Submitted to the Journal of the Electrochemical Society

MATHEMATICAL MODELING OF THE LITHIUM-ALUMINUM, IRON
SULFIDE BATTERY. I. GALVONOSTATIC DISCHARGE BEHAVIOR

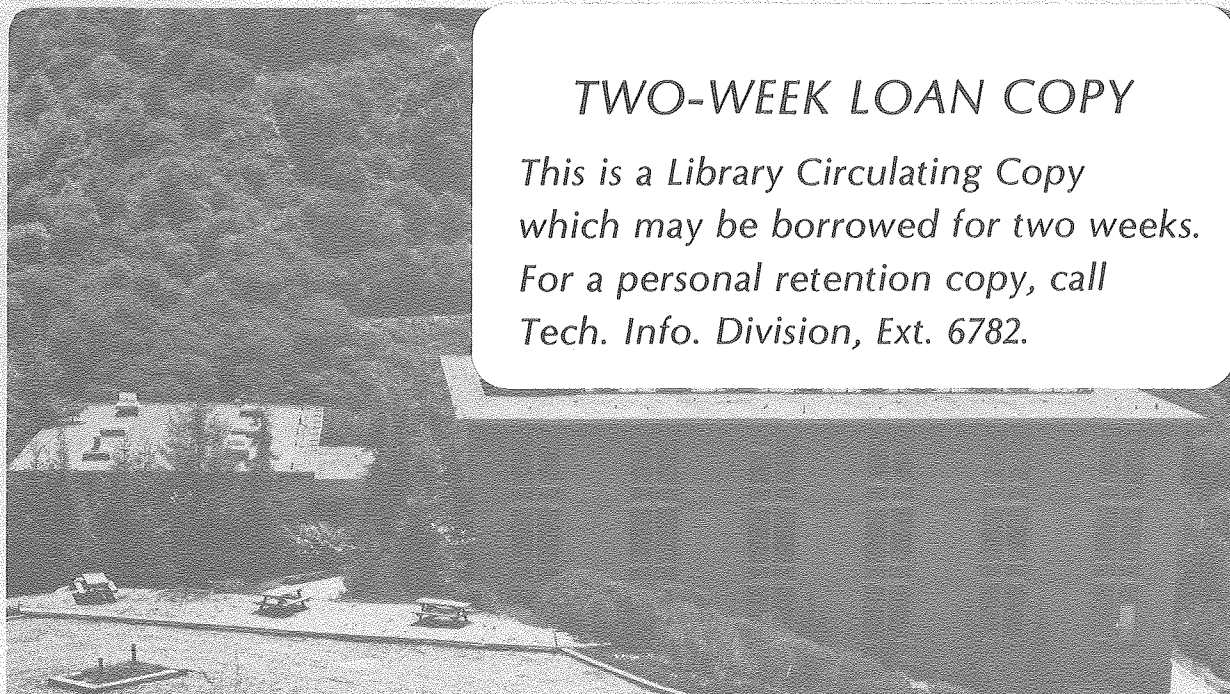
Richard Pollard and John Newman

January 1980

RECEIVED
LAWRENCE
BERKELEY LABORATORY

APR 3 1980

LIBRARY AND
DOCUMENTS SECTION



TWO-WEEK LOAN COPY

*This is a Library Circulating Copy
which may be borrowed for two weeks.
For a personal retention copy, call
Tech. Info. Division, Ext. 6782.*

LBL 10420 C.2

DISCLAIMER

This document was prepared as an account of work sponsored by the United States Government. While this document is believed to contain correct information, neither the United States Government nor any agency thereof, nor the Regents of the University of California, nor any of their employees, makes any warranty, express or implied, or assumes any legal responsibility for the accuracy, completeness, or usefulness of any information, apparatus, product, or process disclosed, or represents that its use would not infringe privately owned rights. Reference herein to any specific commercial product, process, or service by its trade name, trademark, manufacturer, or otherwise, does not necessarily constitute or imply its endorsement, recommendation, or favoring by the United States Government or any agency thereof, or the Regents of the University of California. The views and opinions of authors expressed herein do not necessarily state or reflect those of the United States Government or any agency thereof or the Regents of the University of California.

Mathematical Modeling of the Lithium-Aluminum,
Iron Sulfide Battery

I. Galvanostatic Discharge Behavior

Richard Pollard^{*,1} and John Newman^{*}

Materials and Molecular Research Division, Lawrence Berkeley Laboratory
and Department of Chemical Engineering, University of California,
Berkeley, California 94720

January 1980

ABSTRACT

A mathematical model of the LiAl/LiCl, KCl/FeS high temperature battery is presented. The model considers a whole prismatic cell which consists of negative electrode, separator, electrolyte reservoir, and positive electrode. Physical phenomena described are ohmic potential drop and diffusion potential in the electrolyte, changes in porosity and electrolyte composition due to electrochemical reactions, local reaction rates, and diffusion, convection, and migration of electrolyte. In addition, the analysis includes finite matrix conductivities, variable physical properties, and the possibility of specific simultaneous reactions in the positive electrode. The theoretical results show many of the trends in behavior observed experimentally. The effects of state of charge, initial electrolyte composition, cell temperature, and current density are presented, and factors that can limit cell performance are identified.

* Electrochemical Society Active Member

¹ Present address: Department of Chemical Engineering, University of Houston,
Houston, Texas 77004

Key words: porous electrodes, molten salt electrolyte, cell performance

Introduction

The LiAl/LiCl , KCl/FeS_x high temperature battery is a candidate for off-peak electrical energy storage and for electric vehicle propulsion. A mathematical model is needed to predict the operational characteristics of the system and to assess the influence of changes in design parameters on the cell performance.

Many models have been proposed to describe the behavior of flooded porous electrodes, and current and reaction distributions in a direction perpendicular to the separator have been considered in great detail.¹ The electrode can be regarded as a homogeneous mixture of matrix and electrolyte² or as a single pore, provided that proper averages are taken over a cross-section.^{3,4}

The macrohomogeneous model has been applied to several specific battery electrodes. An analysis of the constant current discharge behavior of electrodes with sparingly soluble reactants, such as the Ag-AgCl and Cd-Cd(OH)_2 couples, has elucidated the relative importance of different failure modes in these systems.³ Transient and failure analyses have also been made of the zinc electrode⁵ and the lead dioxide electrode.^{6,7} An assessment of steady-state composition profiles in lithium/sulfur battery analogues has been made, but the results are restricted to non-porous systems.⁸

Far less effort has been directed towards modeling complete cells and, up until now, only the lead acid cell has been considered in detail.⁹⁻¹² In this paper, a one-dimensional model is presented for the LiAl/FeS system, which is currently being developed at the Argonne National Laboratory.¹³ A whole prismatic cell is considered, consisting of negative electrode, separator, electrolyte reservoir, and positive electrode (see Fig. 1). The model can be used to identify system limitations and to help guide experimental research.

Model Development

The analysis is based on the macroscopic theory of porous electrodes in which the solution and matrix phases are treated as superposed continua without regard for the actual geometric details of the pores.² With this approach, one can obtain a consistent framework for the description of isothermal transport processes in the molten salt electrolyte.¹⁴

A material balance for species i is given by

$$\frac{\partial(\epsilon c_i)}{\partial t} = a j_{in} - V \cdot \underline{N}_i, \quad (1)$$

where \underline{N}_i is the flux of species i in the pore solution averaged over the cross-sectional area of the electrode and where $a j_{in}$ represents the transfer rate of species i from the solid phases to the pore solution per unit electrode volume. In addition, the superficial current density in the pore solution is due to the movement of the charged species:

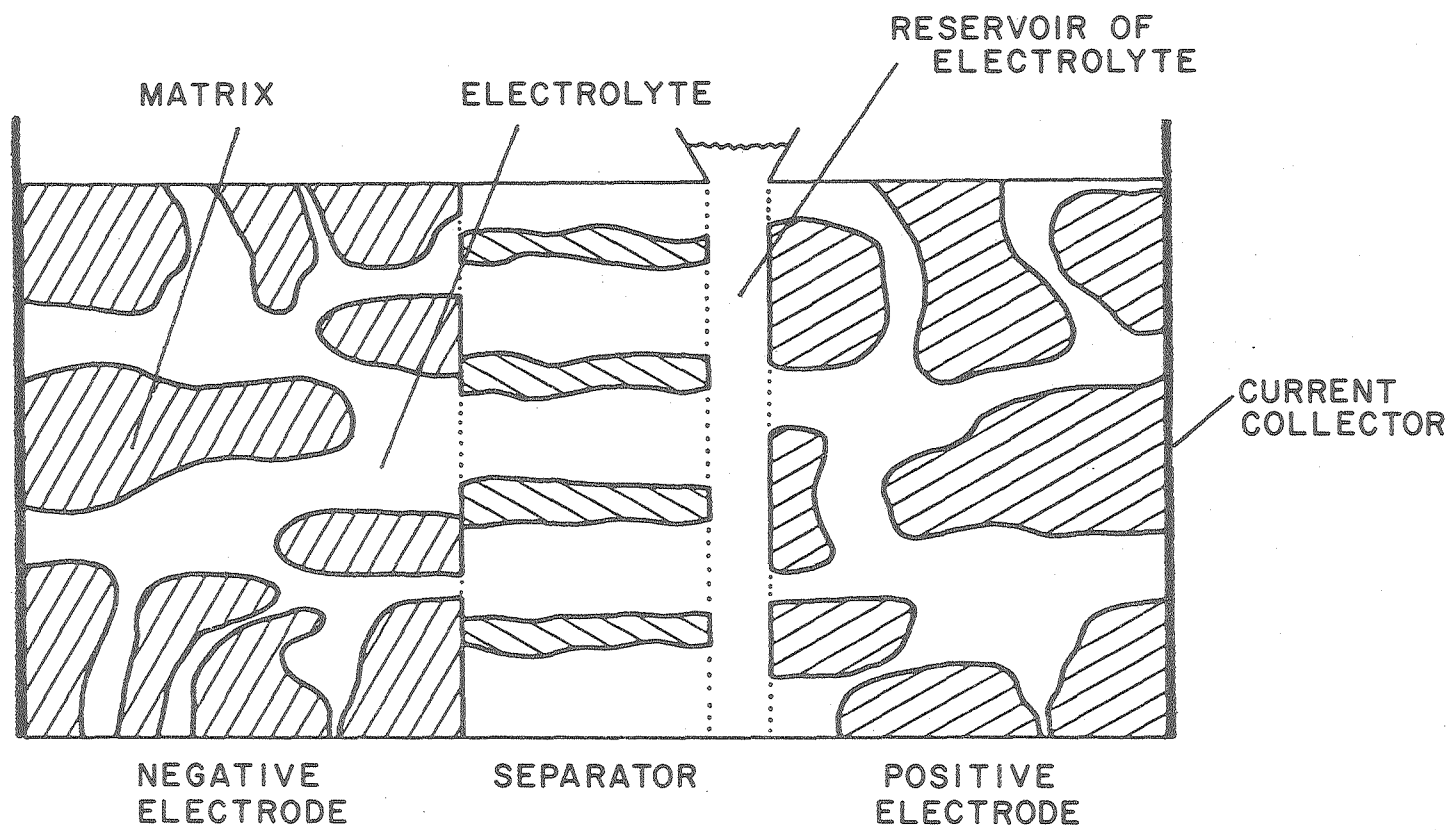


Fig. 1. Schematic diagram of LiAl/FeS cell.

XBL 7910-12435A

$$\underline{i}_2 = F \sum_i z_i N_i \quad (2)$$

and, as a consequence of the condition of electrical neutrality, the divergence of the total current density is zero:

$$\nabla \cdot \underline{i}_1 + \nabla \cdot \underline{i}_2 = 0 . \quad (3)$$

For j simultaneous reactions of the form



Faraday's law can be expressed as

$$a_{j\text{in}} = - \sum_j \frac{s_{ij}}{n_j F} a_{in_j} - \frac{1}{\tilde{V}_k} \frac{\partial \varepsilon_{pk}}{\partial t} , \quad (5)$$

provided that double layer charging can be ignored. The last term on the right side of Eq. (5) represents the removal of species i from the electrolyte as a result of precipitation of salt k . The transfer current per unit electrode volume $\nabla \cdot \underline{i}_2$ is related to the individual average transfer current densities by

$$\nabla \cdot \underline{i}_2 = \sum_j (a_{in_j})_j . \quad (6)$$

A material balance on the solid phases indicates how the electrode porosity changes with the extent of reaction at each location within the electrode:

$$\frac{\partial(\epsilon + \epsilon_p)}{\partial t} = \sum_j \sum_{\substack{\text{solid} \\ \text{phases}}} \frac{s_{ij} \tilde{V}_i}{n_j F} (a_{in})_j, \quad (7)$$

where $\epsilon_p = \sum_k \epsilon_{pk}$.

The flux of mobile species in the electrolyte can be attributed to the combined effects of diffusion, migration, and convention. For the LiCl-KCl electrolyte, the fluxes of lithium and potassium ions are given by:¹⁴

$$\underline{N}_1 = - \frac{\epsilon D}{\tilde{V}} \nabla x_A + \frac{t_1^*}{F} \frac{i}{2} + x_A (c_A + c_B) \underline{v}^*, \quad (8)$$

$$\underline{N}_2 = - \frac{\epsilon D}{\tilde{V}} \nabla x_B + \frac{t_2^*}{F} \frac{i}{2} + x_B (c_A + c_B) \underline{v}^*. \quad (9)$$

These relationships can be substituted into Eq. (1) to give, respectively,

$$\frac{\partial(\epsilon x_A / \tilde{V})}{\partial t} + \nabla \cdot [x_A \underline{g} + (x_B t_1^* - x_A t_2^*) \frac{i}{F} - \frac{\epsilon D}{\tilde{V}} \nabla x_A] = a j_{1n} \quad (10)$$

$$\frac{\partial(\epsilon x_B / \tilde{V})}{\partial t} + \nabla \cdot [x_B \underline{g} + (x_A t_2^* - x_B t_1^*) \frac{i}{F} - \frac{\epsilon D}{\tilde{V}} \nabla x_B] = a j_{2n}, \quad (11)$$

where

$$\underline{g} = \frac{\underline{v}^*}{\tilde{V}} + (t_1^* + t_2^*) \frac{i}{F}. \quad (12)$$

For the special case where $t_1^* = x_A/2$ and $t_2^* = x_B/2$, the direct dependence of Eq. (10) and (11) on current density is removed. The molar average velocity has been chosen as the reference frame because physical data for LiCl-KCl mixtures are often correlated with the mole fraction (see Appendix).

The movement of electrons in the matrix phase is governed by Ohm's law

$$i_1 = -\sigma \nabla \phi_1, \quad (13)$$

where σ is the effective conductivity of the matrix. In the electrolyte, the variation in solution potential is given by

$$\frac{i_2}{\kappa} = -\nabla \phi_2 - \frac{1}{F} \left[\left(\frac{s_1}{n} + t_1^c \right) \frac{1}{x_B} - \frac{s_3 x_A}{n x_B} \right] \nabla \mu_A, \quad (14)$$

where ϕ_2 is measured with a reference electrode that has stoichiometric coefficients s_1 and number n of electrons transferred, and μ_A is the chemical potential of LiCl (see Appendix). Equations (13) and (14) may be combined to obtain variations in the overpotential $\eta = \phi_1 - \phi_2$ directly.

Polarization equations are needed to express the dependence of the local rate of each reaction on the various concentrations and on the potential difference driving force at the reaction interface. Electrode kinetics do not follow fundamental laws that can be expressed as reliably as Ohm's law or the law of conservation of matter. Consequently, the polarization relationships will be subject to further refinement, as one

tries to account not only for the mechanism of the charge transfer process but also for the morphology of the electrode, the formation of covering layers, and the transport of species to and from the reaction site.

It is common to begin with a polarization equation of the form

$$i_{nj} = i_{oj} \left[e^{\alpha_{aj} F \eta_{sj} / RT} - e^{-\alpha_{cj} F \eta_{sj} / RT} \right] \quad (15)$$

where η_{sj} is the local value of the surface overpotential, $\eta_{sj} = \eta - U_{j,o}$, and where the exchange current density can be written as

$$i_{oj} = i_{oj,ref} \prod_i \left(\frac{c_{i,o}}{c_{i,ref}} \right)^{\gamma_i} \prod_k a_k^{\gamma_k} \quad (16)$$

The theoretical open circuit cell potential for reaction j is given by

$$U_{j,o} = U_j^\theta - U_{re}^\theta + \frac{RT}{n_{re} F} \sum_i s_{i,re} \ln a_{i,re} - \frac{RT}{n_j F} \sum_i s_{i,j} \ln a_{i,o} \quad (17)$$

The discharge reaction in the negative electrode is



In the fully charged state, it is assumed that the negative matrix consists of non-porous, spherical particles of β -LiAl. On discharge, the outermost region of a particle reacts first and a layer of α -Al is established which thickens gradually, at the expense of β -LiAl, as the reaction proceeds. The Butler-Volmer equation (15) should be modified to include the diffusional overpotential for mass transport of lithium across the

α -phase to the solid-electrolyte interface.

The parameter

$$S = \frac{3.87(1-\epsilon)I}{nF\bar{c}_{Li} \beta_{La}^2 D_{\alpha}} \quad (18)$$

can be used as a criterion to assess the importance of solid state diffusion within a LiAl particle.¹⁶ Small values of S indicate that the time required for diffusion is much shorter than the time needed for complete utilization of the particle. Even though $S \sim 0(0.1)$ for this system, the influence of solid state diffusion may be appreciable at high current densities or with low specific interfacial areas, particularly towards the end of discharge. However, for $S < 1$, it is reasonable to invoke the pseudo-steady state approximation to evaluate the composition profile within the α -phase. With this assumption, and with unit activity coefficients, the surface concentration of lithium can be written as:¹⁷

$$\frac{(c_{Li}^{\alpha})_o}{(c_{Li}^{\alpha})_{sat}} = 1 - \frac{\nabla \cdot \underline{i}_2}{(\nabla \cdot \underline{i}_2)_{lim}} \quad (19)$$

The diffusion-limited transfer current is given by

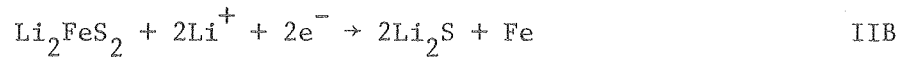
$$(\nabla \cdot \underline{i}_2)_{lim} = \frac{4\pi NFD_{\alpha} (c_{Li}^{\alpha})_{sat}}{(1 - \frac{\alpha}{x_{Li}}) (\frac{1}{r_{\beta}} - \frac{1}{r_{\alpha}})} \quad (20)$$

where r_{α} and r_{β} can be related to the state of charge.¹⁷ Combination of Eq. (6), (15), (19), and (20) gives

$$\nabla \cdot \underline{i}_2 = \frac{e^{\frac{\alpha_a F \eta}{RT}} - e^{\frac{-\alpha_c F \eta}{RT}}}{\frac{1}{4\pi N r_\alpha^2 i_{o,ref} \left(\frac{x_A}{x_{A,ref}} \right)} + \frac{e^{\frac{\alpha_a F \eta}{RT}}}{(\nabla \cdot \underline{i}_2)_{lim}}} \quad (21)$$

where η is measured with a reference electrode of the same kind as the working electrode, but with a fixed lithium activity corresponding to saturated β -phase (see Table 1). Implicit in Eq. (21) are the assumptions that there is no more reaction after the β -LiAl is completely transformed to α -Al and that there are no variations in electrolyte composition between the center of a pore and the adjacent solid surface.

The complicated discharge processes in the positive electrode are represented by two simultaneous reactions:



Equation (15) is used to describe the rate of each reaction, and the reference electrode is taken to be the same kind as reaction IIB (see Table 1). More sophisticated models for the positive electrode kinetics could include additional intermediate reactions, diffusion of reactants and products to and from reaction sites, and crystallization overpotentials for the formation of solid products. However, the detailed mechanism

Table 1. Kinetic parameters used in model

Negative Electrode		Positive Electrode	
Parameter	Value	Value	Parameter
$\alpha_a = \alpha_c$	0.5	1.0	$\alpha_{aj} = \alpha_{cj}$
n	1.0	2.0	n_j
s_1	-1.0	-2.0	$s_{1,j}$
s_3	0.0	0.0	$s_{3,j}$
$(x_A)_{ref}$	0.58	1.0	$(x_A)_{ref}$
γ_{Li^+}	0.5	1.0	γ_{Li^+}
$i_o (A/cm^2)$	2.8	2.0×10^3	$(ai_o)_j (A/cm^3)$
$D_\alpha (cm^2/s)^{30}$	4.0×10^{-10}	0.0326	$U_{IIA,o} (V)$
\bar{x}_{Li}^α	0.05	0.0	$U_{IIB,o} (V)$

of the reactions and the juxtaposition of the different phases have not yet been formally established and are the subject of a separate study.¹⁸ At the high operating temperatures of the lithium/iron sulfide system, and with the relatively high concentration of lithium ions in the electrolyte, the rate of reaction is expected to be high and, therefore, the simplified kinetic analysis may be adequate.

The governing differential equations for the lithium-aluminum/iron sulfide system are subject to the following boundary conditions (see Fig. 1):

(i) at the current collectors;

$$\begin{aligned} (a) \quad \underline{N}_i &= 0, \\ (b) \quad \underline{g} &= 0, \\ (c) \quad \underline{i}_2 &= 0, \end{aligned} \tag{22}$$

(ii) at the negative electrode/separator interface;

$$\begin{aligned} (a) \quad \underline{i}_2 &= I, \\ (b) \quad x_A, \underline{v}^{\star} &\text{ continuous}, \\ (c) \quad \left(\epsilon D \frac{\partial x_A}{\partial y} \right)_s &= \left(\epsilon D \frac{\partial x_A}{\partial y} \right)_e, \end{aligned} \tag{23}$$

(iii) at the positive electrode/reservoir interface;

$$\begin{aligned} (a) \quad \underline{i}_2 &= I, \\ (b) \quad x_A &\text{ continuous}, \\ (c) \quad \frac{V_R}{A} \frac{\partial x_{AR}}{\partial t} &= \left(\epsilon D \frac{\partial x_A}{\partial y} \right)_e - \left(\epsilon D \frac{\partial x_A}{\partial y} \right)_s, \end{aligned} \tag{24}$$

where V_R/A can be estimated from

$$\frac{\partial (V_R/A)}{\partial t} = \frac{v_s^*}{-s} - \frac{v_e^*}{-e} + \frac{V_R}{A} \frac{d \ln \tilde{V}}{dx_A} \frac{\partial x_A}{\partial t} . \quad (25)$$

The electrolyte composition is assumed to be uniform across the reservoir. It should also be noted that alternative formulations can be used for the boundary conditions at the front of the electrodes. These choose control volumes for the material balances that avoid the need for separate evaluation of the composition gradients at the interfaces.¹⁷ In the separator, the governing equations can be simplified in accordance with:

$$\begin{aligned} \text{a) } \underline{i}_2 &= I , \\ \text{b) } \nabla \cdot \underline{i}_2 &= 0 , \\ \text{c) } \epsilon &= \epsilon_s . \end{aligned} \quad (26)$$

The initial conditions are taken as:

$$\begin{aligned} \text{(i) } x_a &= x_A^o , \\ \text{(ii) } \epsilon_e &= \epsilon_e^o , \end{aligned} \quad (27)$$

$$\text{(iii) } \nabla \cdot (\tilde{V} \underline{g}) = \bar{V}_A a j_{1n} + \bar{V}_B a j_{2n} - \frac{\partial \epsilon}{\partial t} + \frac{\epsilon}{\tilde{V}} \frac{\partial \tilde{V}}{\partial T} \frac{\partial T}{\partial t} + \tilde{V} \nabla \cdot \left(\frac{\epsilon D}{\tilde{V}} \nabla x_A \right) ,$$

where Eq. (27(iii)) is derived from Eq. (10) and (11).

During discharge the temperature is assumed to be uniform throughout the cell sandwich but it can change with time in response to reversible heat effects, Joule heating, overpotentials associated with electrode reactions, and precipitation or dissolution of electrolyte.

The first law of thermodynamics gives

$$\frac{\hat{m}\hat{C}_p}{A} \frac{dT}{dt} = [U_o - V - T_o \frac{\partial U_o}{\partial T}]I - h_o(T - T_A) + \sum_k \frac{L_k}{\tilde{V}_k} \int_0^L T \frac{\partial \epsilon_{pk}}{\partial t} dy, \quad (28)$$

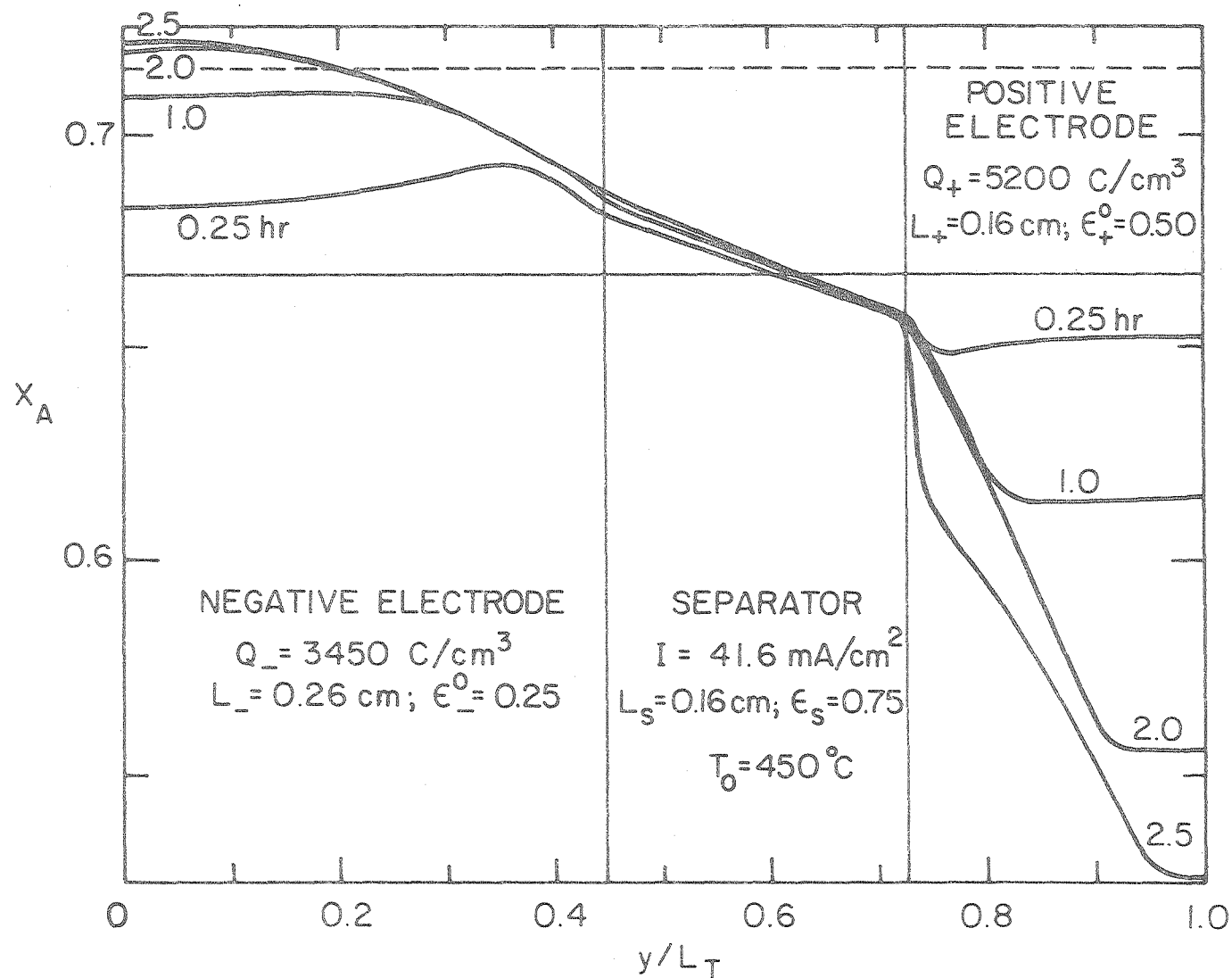
where the heat transfer coefficient h_o is based on estimated heat losses for a battery module.

The LiAl/LiCl, KCl/FeS system can be described by the local variables x_A , ϵ , i_2 , g , and η , and by the governing Eqs. (7), (10), (11), (14), and (15), subject to the specified boundary conditions. These relationships constitute a set of coupled, ordinary, nonlinear differential equations at each time step which are cast into finite difference form accurate to $O(h^2)$, and solved simultaneously by a numerical technique.¹⁹ Each nonlinear equation is linearized properly to assure convergence, and each time-dependent equation is programmed symmetrically between the old time step and the present one, in order to attain stability.

Results and Discussion

Electrolyte Composition

Figure 2 shows composition profiles across the cell sandwich for several times during a constant current discharge of 41.6 mA/cm^2 . A lithium-rich electrolyte is used, and the dimensions and capacities of the fully charged electrodes correspond to those of the Argonne National Laboratory, Mark 1A cell.¹³ When the discharge is started,



-15-

XBL 7910-7169A

Fig. 2. Position dependence of mole fraction of LiCl at different discharge times. Dashed line represents saturation limit for LiCl at 450°C . Simulation parameters: $N = 1.1 \times 10^8 \text{ cm}^{-3}$; Tables 1 and 3.

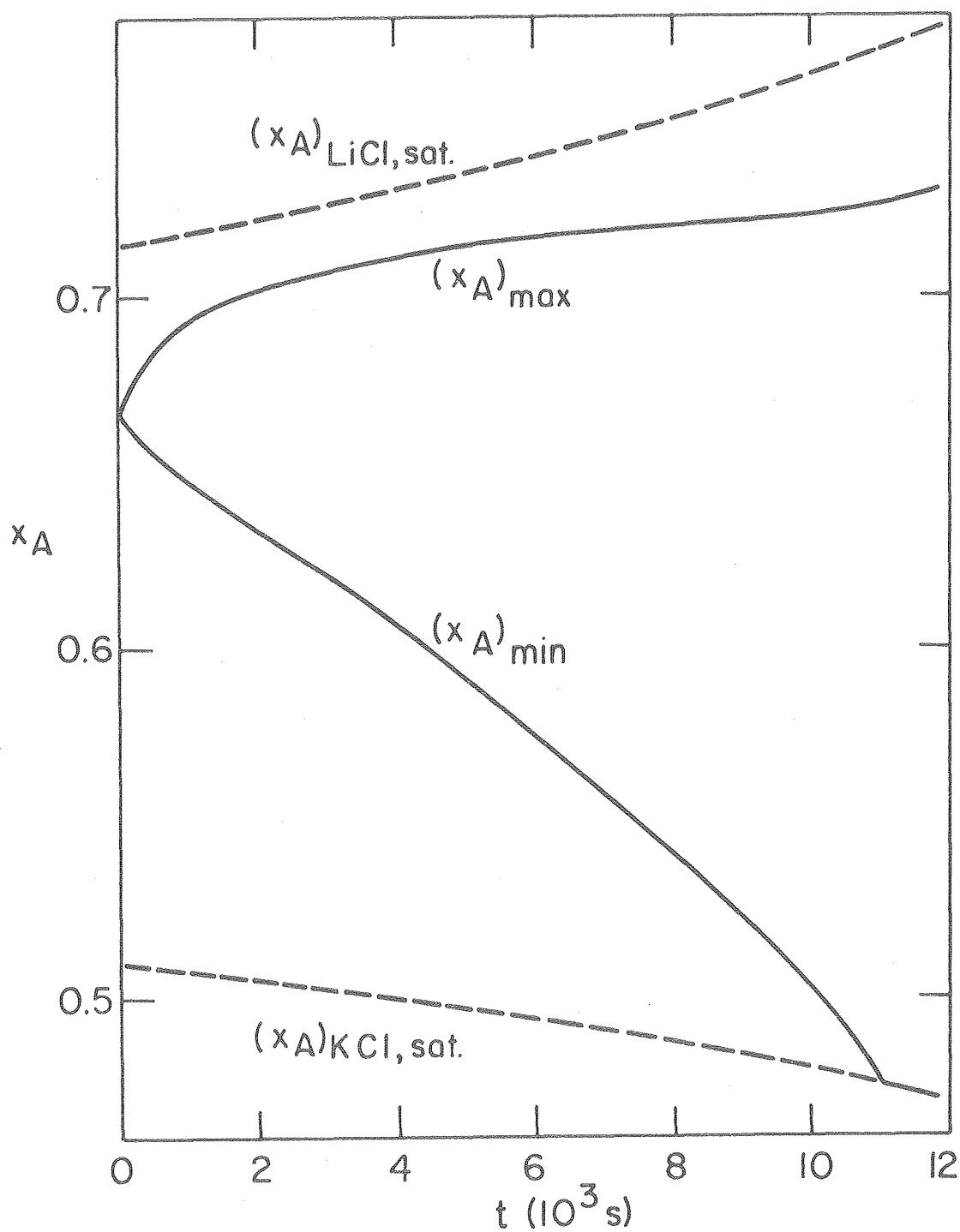
lithium ions are introduced into the electrolyte at the negative electrode and transported across the porous separator to the positive electrode, where they can react cathodically to form Fe and Li_2FeS_2 or Li_2S . Since the transference number of Li^+ is not unity, a concentration profile develops, and diffusion aids migration in the transport of lithium ions. An almost constant composition gradient is established across the separator that corresponds to the flux of lithium ions needed for the specified current density. The presence of the reservoir attenuates composition changes at the front of the positive but, within the electrode, the composition variations are accentuated by local porosity changes.

The details of the composition variations can be attributed to the combined effects of diffusion, migration, convection, and electrochemical reaction. The contribution of convection, which arises primarily from the influx or squeezing out of electrolyte as the porosity alters, is expected to be small for this system ($\underline{v}^* \sim 0(10^{-5})\text{cm/s}$). However, convection is included in the analysis to ensure that the accuracy of the electrolyte material balances is retained.

The importance of \underline{v}^* was tested by repeating the simulation in Fig. 2, with the temperature dependence of the electrolyte molar volume included in a manner that caused oscillation in \underline{v}^* , without adversely affecting the material balances. The results differed by less than 0.2%, except in the region with KCl precipitation, where the largest error in ϵ_p was 5%. The sensitivity of precipitation to temperature and composition indicates that a significant proportion of this error should be associated with changes in \tilde{V} , rather than \underline{v}^* .

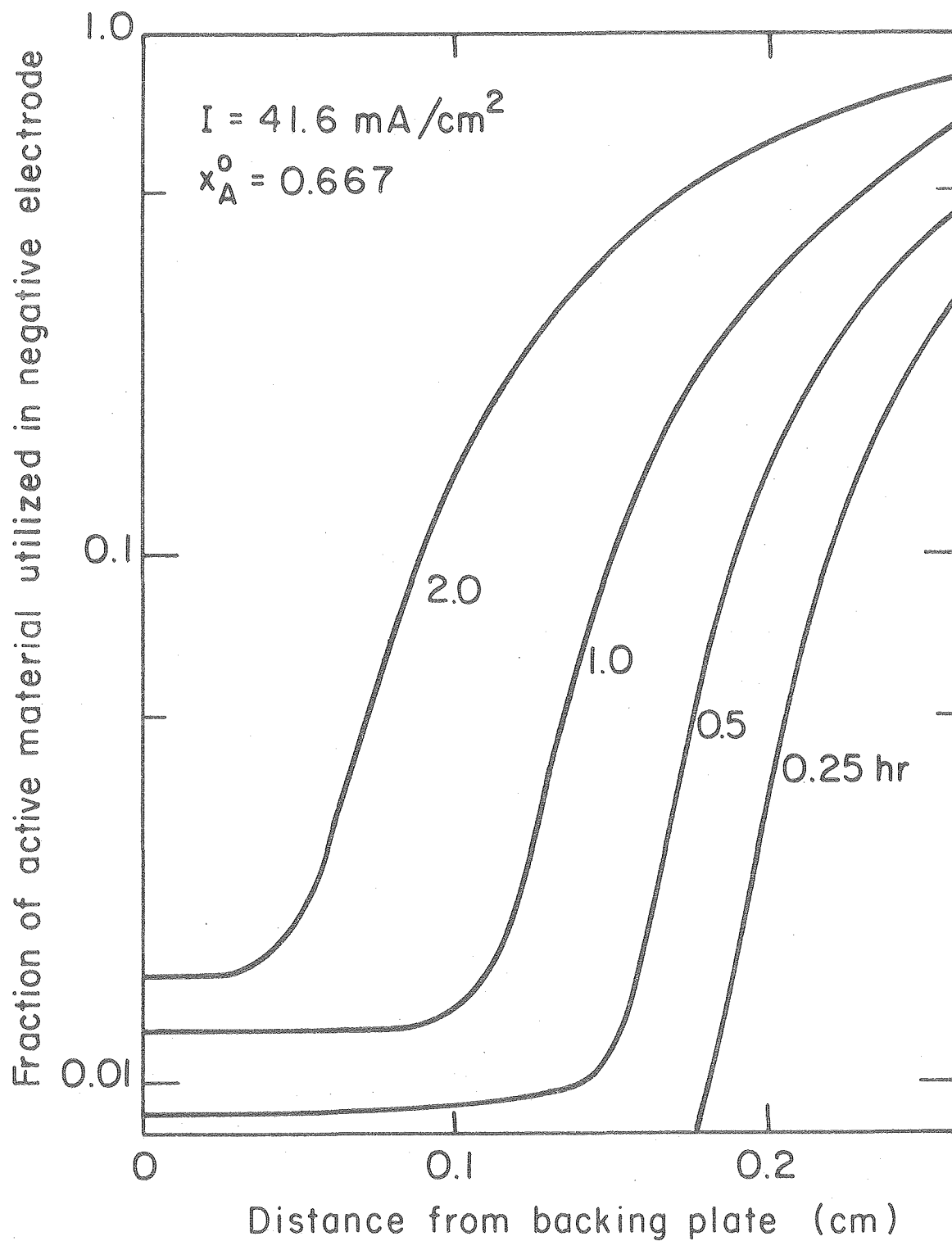
If the cell temperature remains constant, the model predicts that the electrolyte composition in the negative electrode would cross the solubility limit for LiCl (indicated by the dashed line) after 1.5 hours. However, the average temperature rises by approximately 15°C during this period, and therefore precipitation of LiCl is avoided. Nevertheless, at about 54% depth of discharge, the composition has fallen markedly in the positive electrode and precipitation of KCl is predicted. This is illustrated in Fig. 3, which shows the variations in maximum and minimum electrolyte concentrations during the discharge, in comparison with the saturation compositions. The prediction of large variations in electrolyte composition during discharge emphasizes the need for inclusion of variable physical properties in the theoretical analysis.

The fraction of active material utilized within the negative electrode is shown in Fig. 4, at several discharge times. The large electrode surface area and the high operating temperature help to create fast reaction kinetics. As a result, a highly nonuniform reaction distribution, dominated by ohmic effects, is obtained. Initially, the sharp reaction front is restricted to the electrode/separator interface because an infinite matrix conductivity has been assumed for the simulation.^{2,20} This reaction zone gradually moves through the electrode as active material is consumed and the potential required for the reaction becomes more positive. At the back of the electrode, the transfer current rises gradually in response to the composition-dependent term in the Ohm's law relationship for the electrolyte. This effect is more pronounced at high current densities and, as a result,



XBL7912-14577

Fig. 3. Comparison of variations in saturation limits for LiCl and KCl and maximum and minimum electrolyte concentrations. Parameters as in Fig. 2.



XBL 7910-7166A

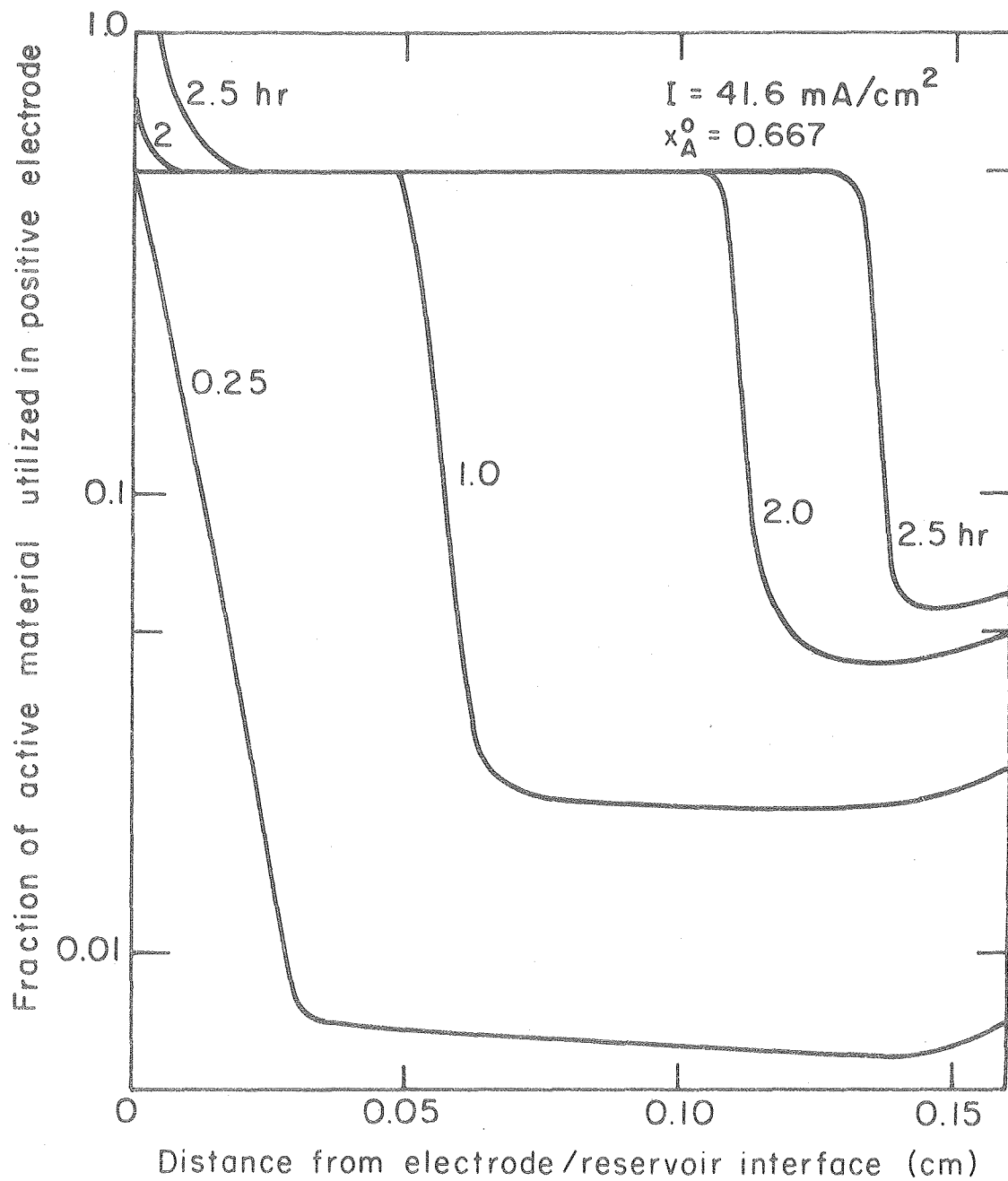
Fig. 4. Fraction of active material utilized in negative electrode at different discharge times. Parameters as in Fig. 2.

the reaction front at a given state of charge is less sharp at higher discharge rates.

The complementary reaction distributions for the positive electrode are presented in Fig. 5. Reaction IIA starts first, and after two hours it has proceeded about two-thirds of the way through the electrode. The FeS is fully converted to Li_2FeS_2 behind this reaction front, which is itself relatively narrow. Subsequently, a front for reaction IIB begins to move through the electrode, and its influence on the composition can be seen in Fig. 2 at 2.5 hours.

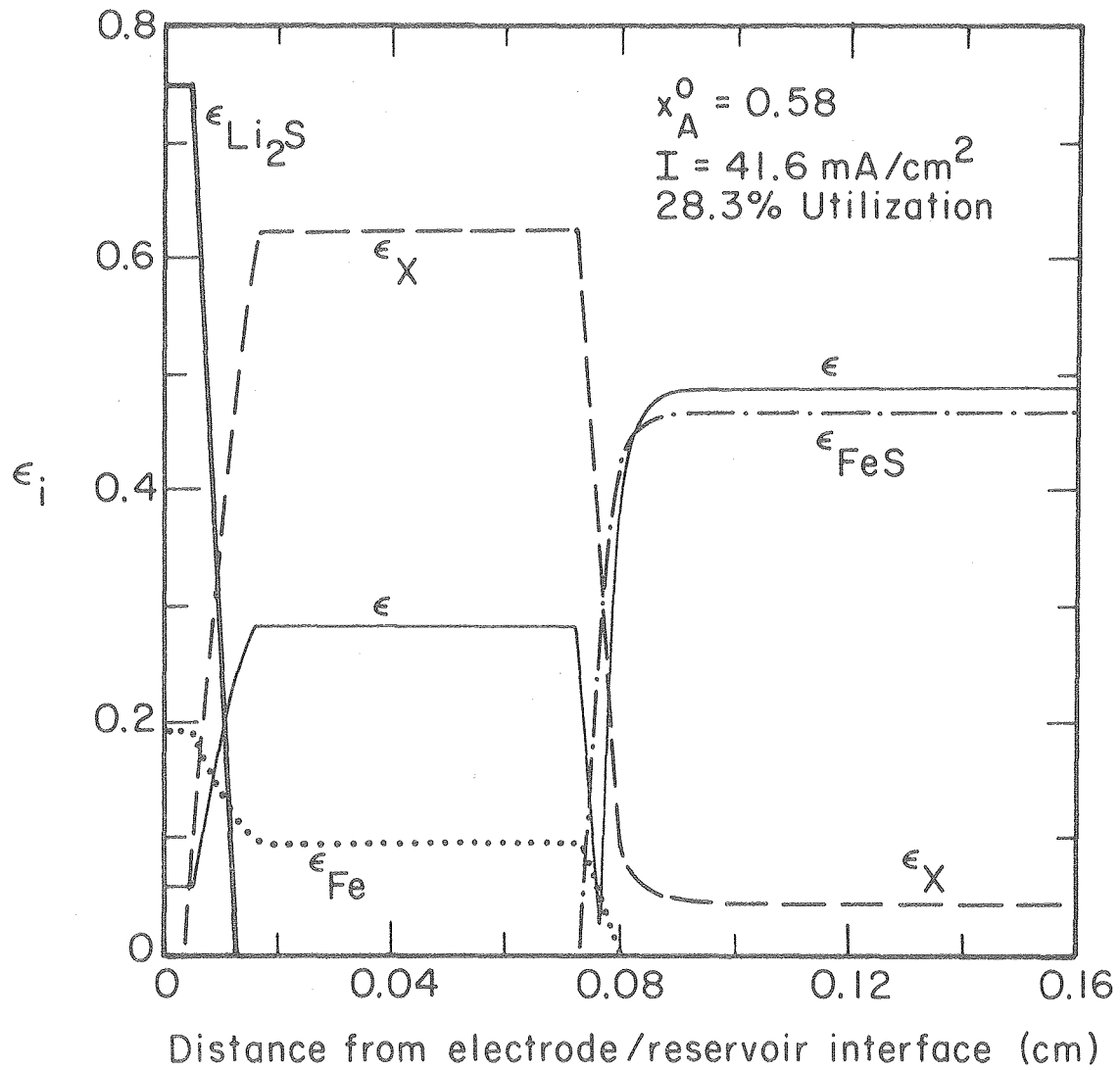
The distance that the first reaction penetrates the electrode before onset of the second front is dependent on the operating conditions. Table 2 indicates that the distance between the fronts is smaller, and hence the reactions are less distinct, with higher current densities or with lower initial electrolyte compositions.

The microstructure in the positive shortly after the second reaction has begun is shown in Fig. 6. In this example, the initial composition is that of the eutectic, 58 mole percent LiCl, and precipitation of KCl occurs at a relatively low depth of discharge. Precipitation is responsible for the extremely small value of the porosity ϵ at a distance of about 0.075 cm which effectively blocks off the back portion of the electrode. In this isolated region, self-discharge reactions can take place as a result of composition variations in the electrolyte and potential gradients in the matrix. The diagram shows that, in the depth of the electrode, reaction IIA has occurred to some extent, producing a certain volume fraction ϵ_X of Li_2FeS_2 and slightly



XBL7910-7167A

Fig. 5. Fraction of active material utilized in positive electrode at different discharge times. Parameters as in Fig. 2.



XBL 7910-12434 A

Fig. 6. Volume fractions of solid phases and electrolyte in positive electrode. Parameters as in Fig. 2, except as indicated.

Table 2. Characteristics of reaction fronts in positive electrode.

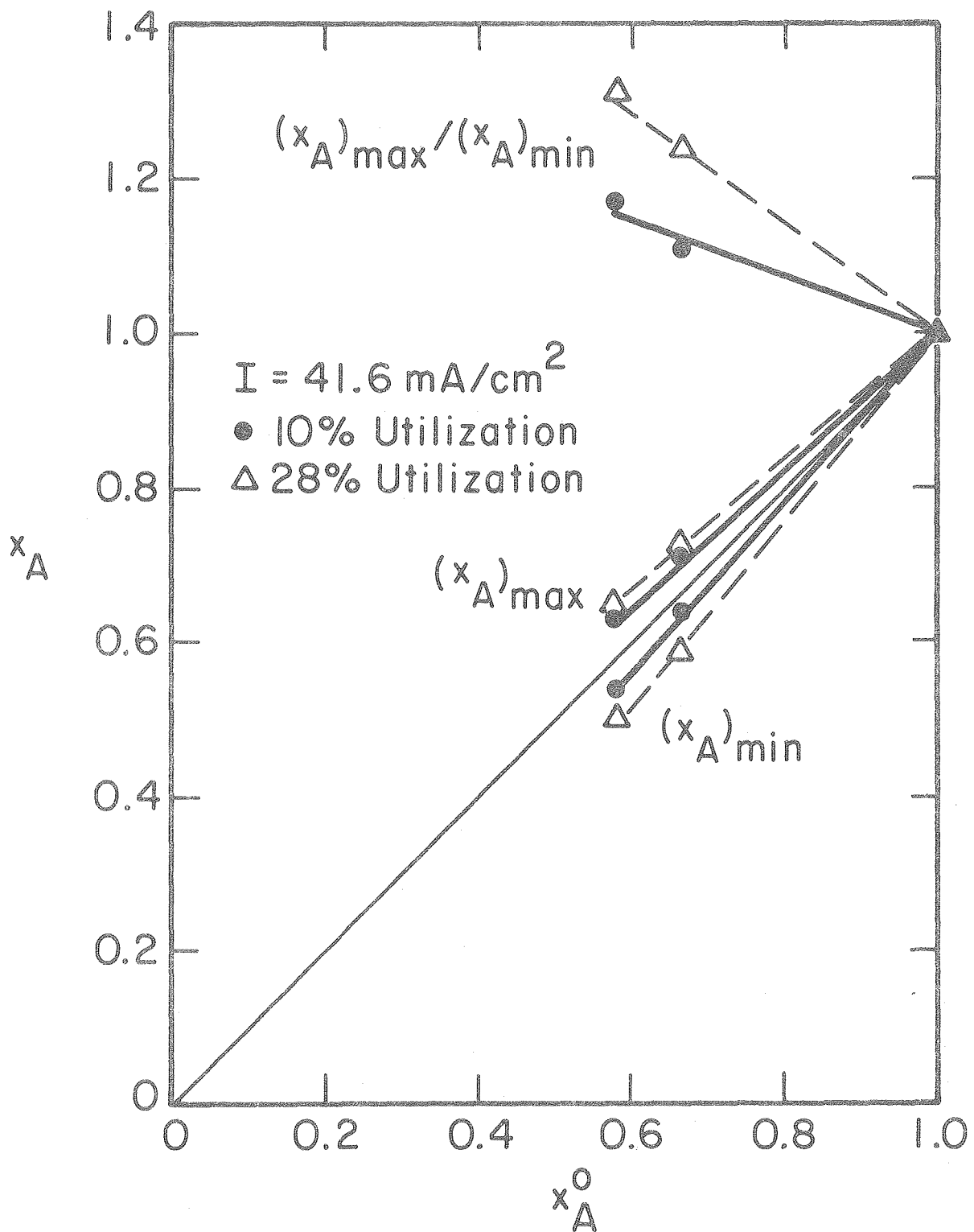
x_A^o	0.58		0.667	
$I(A/cm^2)$	0.0416	0.1	0.0416	0.1
L_{gap}/L_+	0.40	0.18	0.63	0.30
$100t_{f2}/t_f$	22.7	12.2	33.6	17.7

decreasing the porosity from its initial value of 0.5. Behind the central reaction front, there is a plateau for the values of ϵ_X , ϵ , and ϵ_{Fe} that corresponds to completion of reaction IIA. At distances less than 0.01 cm from the reservoir, the consequence of reaction IIB can be seen; Li_2FeS_2 is consumed, Li_2S is produced, and the porosity drops to a small value.

As the first reaction front moves back through the positive electrode, the precipitated region does so also, and it remains as a sharp spike located in the region of highest transfer current. The progression of the second reaction is accelerated by the isolation of the back of the electrode and the region of precipitation can spread rapidly to affect a larger part of the electrode. The local reductions in porosity that result from the large molar volume of the Li_2S and the precipitation of KCl lead to a reduction in local electrolyte conductivity in accordance with Eq. (32). Consequently, a significant potential drop can develop across the low porosity region, and this may severely limit utilization of the electrode. The plugging of porous electrodes has been cited as a possible cause of failure in other electrodes.^{5,21} In the zinc electrode, for example, a large volume fraction of ZnO can be produced at the front face early in a discharge, particularly if the reaction distribution is highly nonuniform.

Initial Electrolyte Composition

An important consideration in the development of the LiAl/LiCl, KCl/FeS battery is the choice of initial electrolyte composition, x_A^0 . The dependence of composition changes on x_A^0 is illustrated in Fig. 7,



XBL 7912-13698

Fig. 7. Dependence of composition variations on initial electrolyte concentration. Parameters as in Fig. 2, except as indicated.

at two different depths of discharge. The difference between the maximum and minimum electrolyte compositions is larger for smaller x_A^0 , and this effect becomes magnified as the discharge proceeds. The composition changes have a direct influence on the extent of precipitation and on the Nernst relationship for the cell potential.

With pure LiCl, there is no concentration polarization, but the minimum operating temperature would be 609°C. For molten salt mixtures with Li^+ as a common ion, the composition changes in the Li/FeS cell are expected to be small. The transport theory developed in reference 14 can be applied directly to binary electrolytes such as LiCl-LiF. It also applies to more complicated mixtures, such as LiCl-LiF-LiBr, provided that it is reasonable to assume that, from a mass transport standpoint, the anions can be lumped together to give only a single independent composition variable.

If the anions do not participate in the electrode reactions, the production term in the material balance equation is given by¹⁴

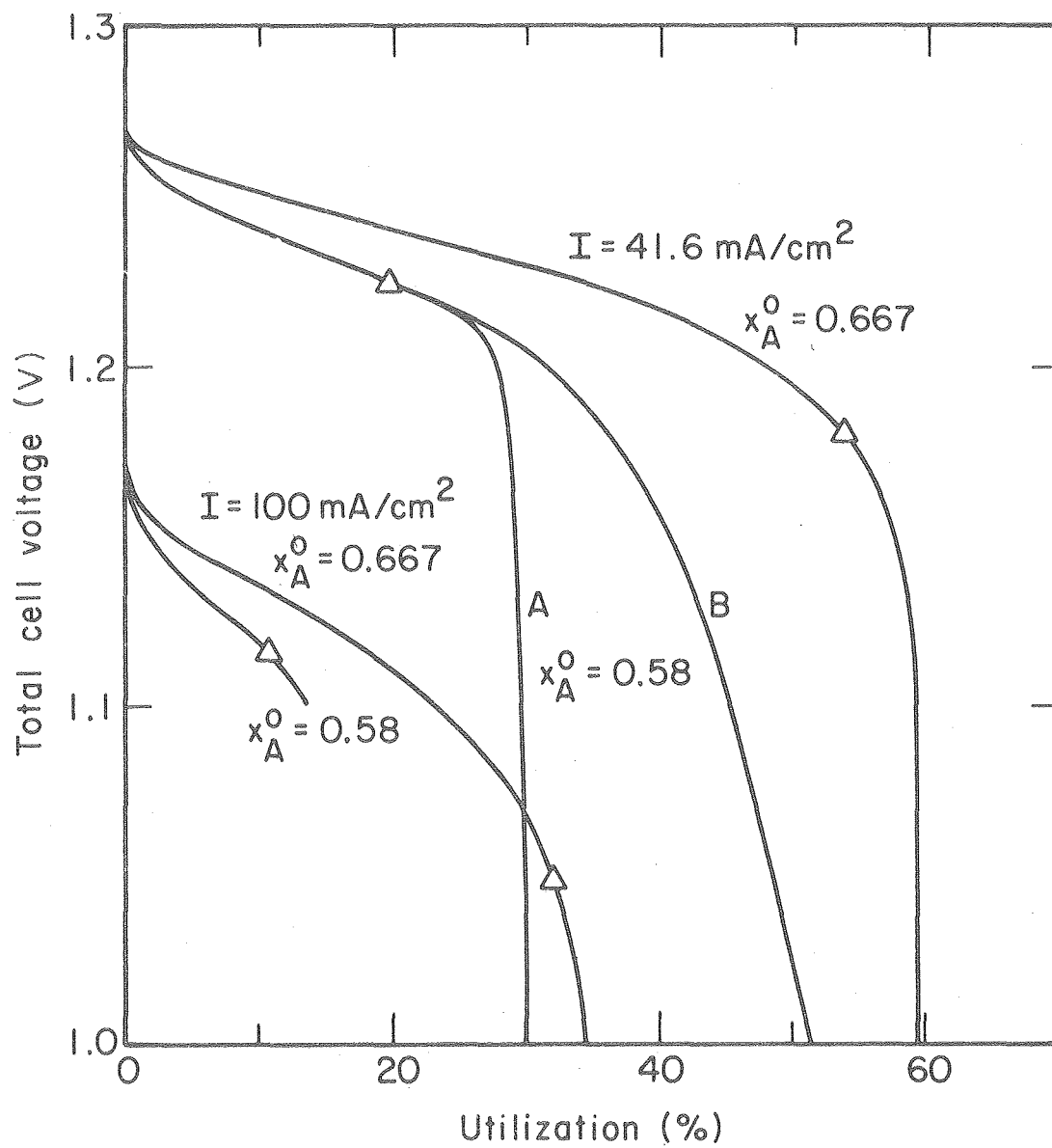
$$R_A = \tilde{V} a j_{3n} \left(\frac{c_2 t_1^r}{v_2^B v_3^A} - \frac{c_1 t_2^r}{v_1^A v_3^B} \right) . \quad (29)$$

For electrolytes with unit stoichiometric coefficients, and for transference numbers that are directly proportional to concentration, Eq. (29) reduces to $R_A = 0$ and, therefore, the electrolyte composition is constant. In practice, R_A is still expected to be small even with transference numbers not exactly proportional to concentration, and

successful cell operation may be possible at temperatures much closer to the melting point than are permissible with the LiCl-KCl electrolyte.

Discharge curves

An important capability of the model is to predict the dependence of total cell voltage on state of charge. Discharge curves for the Argonne Mark 1A cells are presented in Fig. 8 for several different operating conditions. The upper curves are for a current density of 41.6 mA/cm^2 , and the highest of these is for a lithium-rich electrolyte, which has a larger bulk electrolyte conductivity than the eutectic mixture. Two curves are shown for the eutectic, which is the composition actually used in the Mark 1A cell design. Curve A takes account of precipitation of either component of the electrolyte, whereas curve B does not. For all three curves, the sharp reduction in cell voltage can be attributed to the localized porosity reductions in the fully reacted region of the positive electrode. Precipitation reduces the porosity still further, and the decline in voltage is correspondingly more acute. In practice, the porosity changes may not be quite so dramatic because it is possible for the electrodes to swell. Expansion may occur by compaction of the separator and displacement of the can walls during the formation cycles of the cell, or by motion of the electrodes relative to one another during a particular charge or discharge. The extent to which swelling can take place will depend on the stresses generated within the cell and the physical restraints on the container.



XBL 7910-12253 A

Fig. 8. Theoretical discharge curves for Argonne National Laboratory Mark 1A cells. Parameters as in Fig. 2, except as indicated.

At the high current density, the initial cell voltage is considerably reduced as a result of the finite grid resistance (see Appendix). Also, the cell voltage declines more rapidly since there is less time available for diffusional processes to take place, and because the reaction distribution in the positive electrode is less uniform (see Table 2).

The triangles in Figure 8 indicate the onset of precipitation of KCl. They show that, at lower I or higher x_A^O , precipitation is delayed. The exact time when precipitation begins is largely dependent on the details of the heat balance used to estimate the average cell temperature, Eq. (28). Small changes in the rate of heat loss from the battery module, or slight differences in initial cell temperature, could have a significant impact on the extent of precipitation and, possibly, on the cell performance. In the examples shown, precipitation of LiCl is not predicted, even though the maximum composition is close to the solubility limit (see Fig. 3).

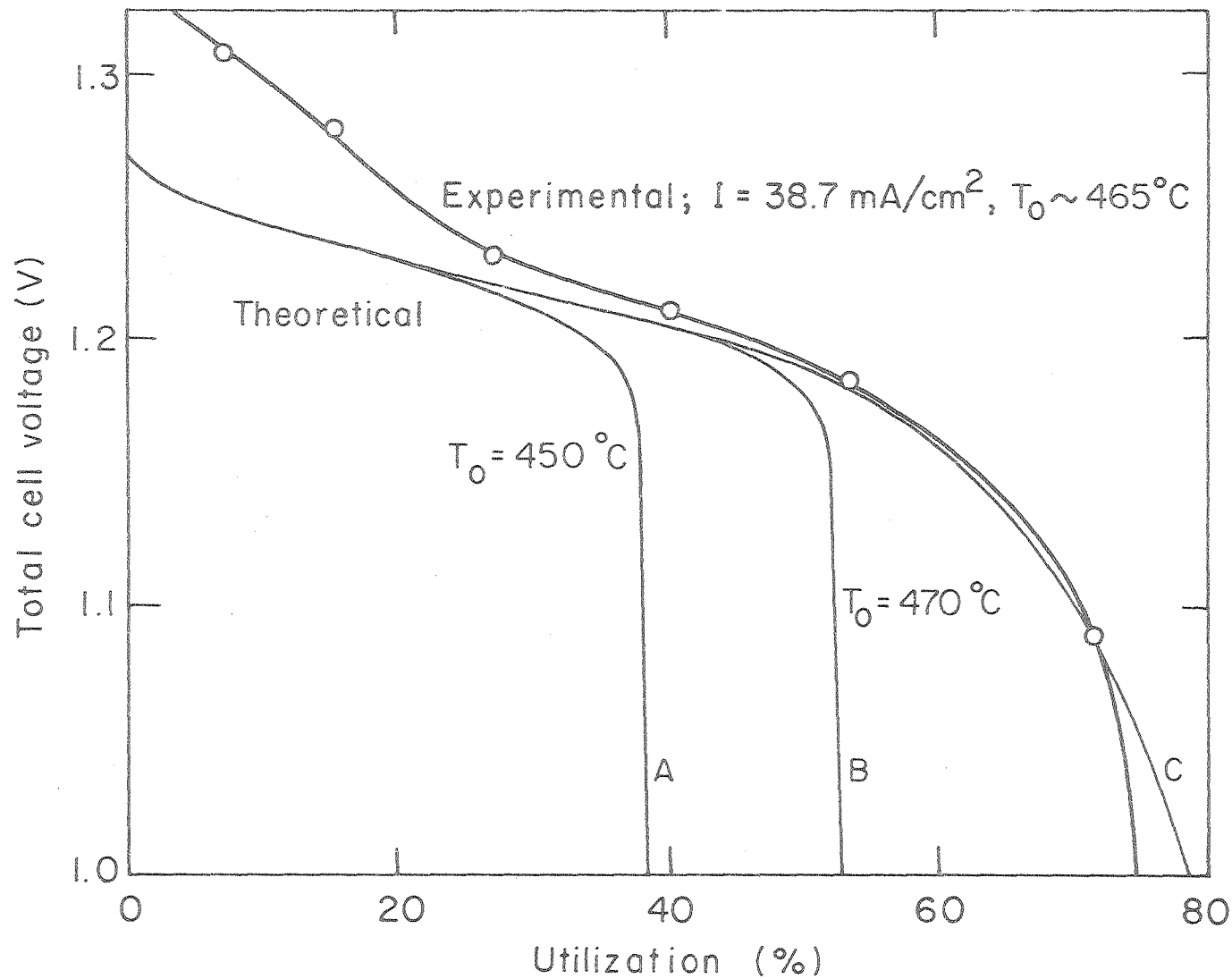
Careful consideration of precipitation is needed for several additional reasons. The rate of mass transport from the electrolyte in the bulk of the pores to the matrix surface may influence the rate at which precipitation takes place. This has been included in previous studies of electrodes with sparingly soluble reactants,²²⁻²⁴ but the effects may not be so important in molten salt systems because the salt concentrations are generally much higher. The morphology of the precipitate may be important, particularly if it forms as a passivating layer over the active material. Furthermore, local thermal effects

may influence the extent and nature of precipitation; heat generated as precipitate forms will tend to retard the precipitation process.

In Fig. 9, an experimental discharge curve is compared with theoretical predictions obtained at a similar current density. The experiment was done with a bicell (2 negative electrodes with a central positive plate) that was built with electrodes designed for the Mark 1A battery program.²⁵ The computer simulation is based on the electrode capacities specified in Fig. 8, but it is assumed that the positive and negative electrodes have expanded 12.5% and 23%, respectively. It is also assumed that the heat transfer coefficient h_o is twice as large as the value assumed for the Mark 1A battery model. The ambient temperature used in the model remains at 25°C, whereas it may be closer to 450°C in the experiments.

Theoretical curves A and B in Fig. 9 indicate the influence of initial cell temperature on the predicted system behavior. The cell temperatures rise by 18°C and 26°C during the discharge, for low and high T_o , respectively. Even with high operating temperatures and swollen electrodes, the maximum predicted utilization is still considerably below the experimental observations. Two possible reasons for this discrepancy are:

- a) Larger local porosities in the positive electrode at a given stage of charge due to:
 - (i) additional expansion,
 - (ii) solid phase intermediates with relatively low molar volumes that are not included in the present model,



-31-

XBL 7912-14571

Fig. 9. Comparison of theoretical and experimental²⁵ discharge curves. Simulation parameters: $Q_- = 2800 \text{ c/cm}^3$, $Q_+ = 4630 \text{ c/cm}^3$, $L_- = 0.32 \text{ cm}$, $L_S = 0.16 \text{ cm}$, $L_+ = 0.18 \text{ cm}$, $\epsilon_-^0 = 0.39$, $\epsilon_S^0 = 0.75$, $\epsilon_+^0 = 0.555$, $x_A^0 = 0.58$, $I = 41.6 \text{ mA/cm}^2$, $N = 5.5 \times 10^7 \text{ cm}^{-3}$, $h_0 = 8.25 \times 10^{-2} \text{ W/m}^2 \cdot \text{K}$.

- (iii) more uniform distribution of reactions,
- b) Reduction in amount of KCl precipitation due to:
 - (i) Smaller composition variations as a result of larger porosities or free convection,
 - (ii) high local temperatures,
 - (iii) mass transport limitations,
 - (iv) modification of the equilibrium solubility limit by the presence of sparingly soluble species in the electrolyte or due to supersaturation.

Curve C in Fig. 9 represents the same simulation as curve B , except that precipitation of electrolyte is not taken into account. The relatively good agreement with the experimental data, although possibly fortuitous, gives some support to the reduced precipitation concept and provides an incentive for a more detailed examination of the possible causes enumerated above. In particular, a force balance on the electrolyte in a direction parallel to the separator, together with Darcy's law, indicates that free convection is even less important than forced convection in vertical LiAl/FeS cells.

In addition, at the end of the simulation depicted by curve C in Fig. 9, $(x_A)_{\min} = 0.220$, whereas $(x_A)_{\text{sat}} = 0.437$. If local temperature effects dominated, the temperature in the positive electrode would need to be 155 K above the average cell temperature; temperature differentials of this magnitude are not expected to be observed in these cells because the electrodes are thin and the materials have relatively high thermal conductivities. Furthermore, large degrees of supersaturation

would not be expected in the heterogeneous electrode medium. A separate study may be needed to monitor cell temperature and to investigate local variations in electrolyte composition, under closely controlled experimental conditions.

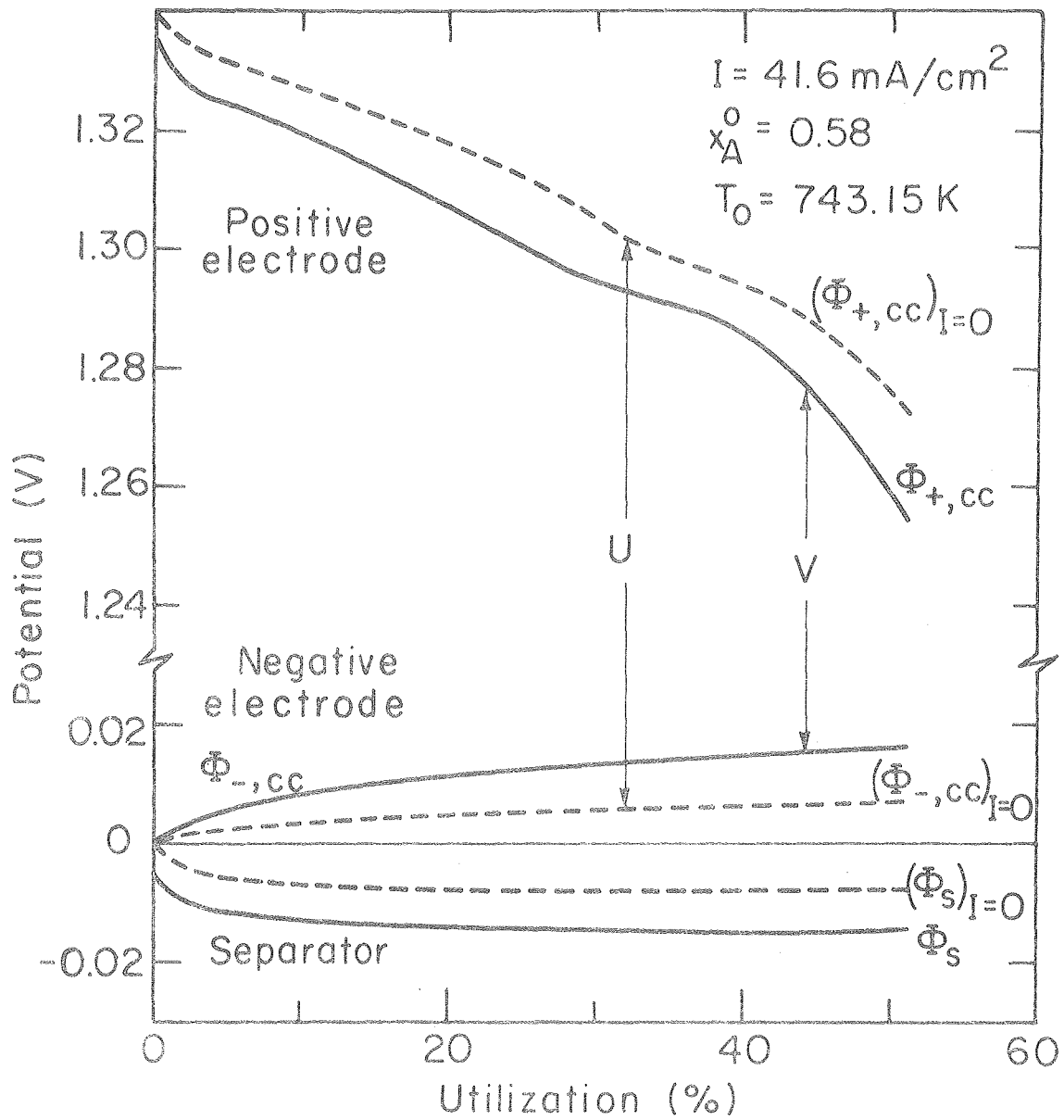
One can also speculate on the reasons for the differences between experiment and theory shown in Fig. 9, at low utilizations. The experimental curve rises more sharply than the model predictions at depths of discharge below approximately 25%. This can be attributed, at least in part, to the presence of about 15% Cu_2S in the positive electrode. Copper sulfide was added to the Mark 1A electrodes to minimize the formation of an intermediate sulfide, $\text{LiK}_6\text{Fe}_{24}\text{S}_{26}\text{Cl}$ (J-phase), which can adversely affect cell performance.²⁶ There is now evidence to suggest that J-phase can also be suppressed by the use of lithium-rich electrolytes and increased operating temperatures.²⁷ Elimination of Cu_2S from the positive would be advantageous because gross movement of Cu_2S to the separator, with subsequent cell shorting, can take place.²⁸

Small quantities of lithium are sometimes added to the negative to augment the electrode capacity. As with Cu_2S , addition of lithium tends to raise the total cell voltage. However, the lithium activity is increased, and this may cause operational difficulties, such as displacement of potassium from the electrolyte, reaction with the separator material, dendrite formation, shift of charge range in cycling, or failure to achieve full charge.

The small discrepancy between experiment and theory at approximately 30% utilization could result, amongst other reasons, from

uncertainty in the estimation of the current collector and terminal resistance (see Appendix). The finite conductance of the grid will also lead to nonuniform current and potential distributions across the face of an electrode, which are not included explicitly in the one-dimensional cell model. A separate study has been made of ohmic drop in current collectors in order to help provide a rational basis for scale-up of cells.²⁹

An analysis of local variations in potential across the cell sandwich can provide additional insight into the behavior of the individual electrodes. Figure 10 shows potentials at different positions across the cell described in Fig. 9, relative to a saturated β -LiAl/LiCl, KCl reference electrode placed at the front face of the negative. The separator potential Φ_s is almost unchanged throughout the discharge, in keeping with the constancy of the composition profile across the separator (see Fig. 2). The open circuit potential difference $(\Phi_s)_{I=0}$, that would be measured by a reference electrode at the front face of the positive electrode, indicates the influence of concentration polarization, which is characterized by the composition dependent term in Ohm's law, Eq. (14). The curves marked $\Phi_{+,cc}$ and $\Phi_{-,cc}$ represent the potentials of the positive and negative current collectors, respectively. The difference between these potentials and their open circuit counterparts can be regarded as the resistances of the individual electrodes. In the negative electrode, there is assumed to be no potential difference in the matrix phase, and, in the positive electrode, the matrix potential difference is too small to be discernable in Fig. 10 because



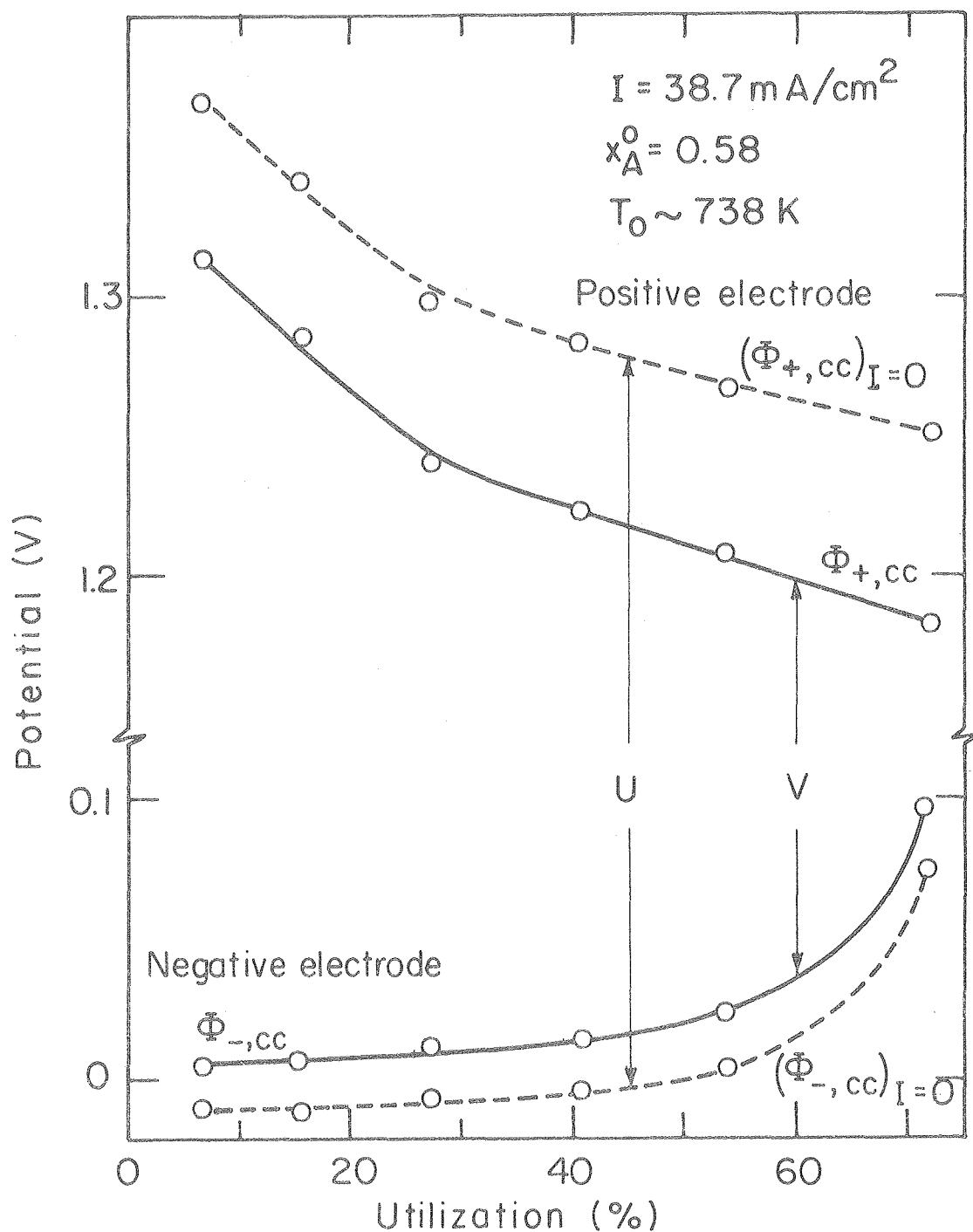
XBL7912-14568

Fig. 10. Theoretical potential variations at different locations across the cell sandwich. Parameters as in Fig. 9. Dashed lines represent open circuit potentials.

the effective matrix conductivity calculated with Eq. (40) is large ($\sigma \sim 0(10^4)\Omega^{-1}\text{cm}^{-1}$), throughout the discharge.

The components of the potential for the experimental cell depicted in Fig. 9 are presented in Fig. 11.²⁵ Both experimental and theoretical results indicate that changes in total cell voltage are largely dependent on the variations in apparent open circuit cell potential U , and that changes in electrode resistances are relatively small. The experimental results show that the positive is polarized more strongly than the negative electrode, but that the negative electrode potential rises more sharply towards the end of discharge. This could be interpreted as a negative electrode 'limitation', although this term has not been carefully defined. In this context, it is not possible to distinguish between limitations caused by inherent electrochemical factors or by changes in the useable capacity of an electrode over a number of cycles. It might be expected that, with a sufficient increase in excess capacity in the negative electrode, the positive would limit cell performance on both charge and discharge.

For both electrodes, the model predicts resistances that are smaller than the observed values. This could be caused by over-estimation of electrochemically active interfacial areas, exchange current densities, or matrix conductivities. Contact resistance or partial loss of electrical connectivity between electrode particles can lead to conductivities below those calculated from Eq. (40), which is based on the concept of parallel conduction paths. Separate experiments may be needed to establish the conductivity of each electrode



XBL 7912-14576

Fig. 11. Potentials at different locations across a cell sandwich measured with a reference electrode placed at the edge of the separator.²⁵ Dashed lines represent open circuit potentials, 15 s after current interruption.

matrix as a function of stage of charge. Contact resistances are not expected to be significant in the positive electrode during discharge because the large volume of solid products tends to increase the internal electrode pressure. Furthermore, the presence of Li_2S at the front of the positive electrode may not influence cell behavior markedly, since all the current will be carried in the electrolyte across the fully reacted region. However, the formation of a poorly conducting layer adjacent to the current collector could have a more profound effect on the predicted potential distribution.

Despite the underestimates for the electrode resistances, the model still gives voltages that lie below the experimental results in Fig. 9. This is directly associated with the estimated value of the current collector resistance R_g , which is only included in the model to improve the accuracy of the heat balance. The estimate of R_g could be refined with more precise experimental data for the polarization conductance Y of a cell element. This parameter (Y) could be obtained directly in a small, open test cell with current collectors large enough to ensure insignificant current and potential variations across the face of a plate and with voltage taps placed in direct contact with the current collectors.

Additional experiments may also be needed to elucidate the reasons for the observed rise in potential of the negative electrode towards the end of discharge (see Fig. 11). The theoretical calculations indicate that the increase in porosity as the discharge proceeds more than compensates for the additional distance the current must penetrate

the electrode, and that the current collector potential approaches a constant (see Fig. 10). The discrepancy between theory and experiment may result from:

- (a) reduction in negative electrode porosity caused by expansion of the positive,
- (b) gross morphology changes in the negative electrode,
- (c) reduction in the available electrode capacity and uncertainty in the state of charge caused by
 - (i) segregation of active material from the bulk
 - (ii) cumulative coulombic losses,
- (d) nonuniform initial distribution of reactants.

Agglomeration would reduce the electrochemically active interfacial area and increase the diffusion overpotential for transport of lithium atoms across the α -Al. A computer simulation with the initial particle size r_o^0 increased by a factor of 4.5 shows an increased electrode resistance at a particular depth of discharge but, contrary to observations, the open circuit potential $(\Phi_{-,cc})_{I=0}$ does not alter appreciably. The influence of the initial variation in state of charge across the negative electrode could be investigated by comparing potential distributions obtained during two experiments; one where a considerable time interval was introduced between the discharge of interest and the previous charge, and the other where the discharge followed the charge immediately, but the overall initial state of charge matched the first experiment.

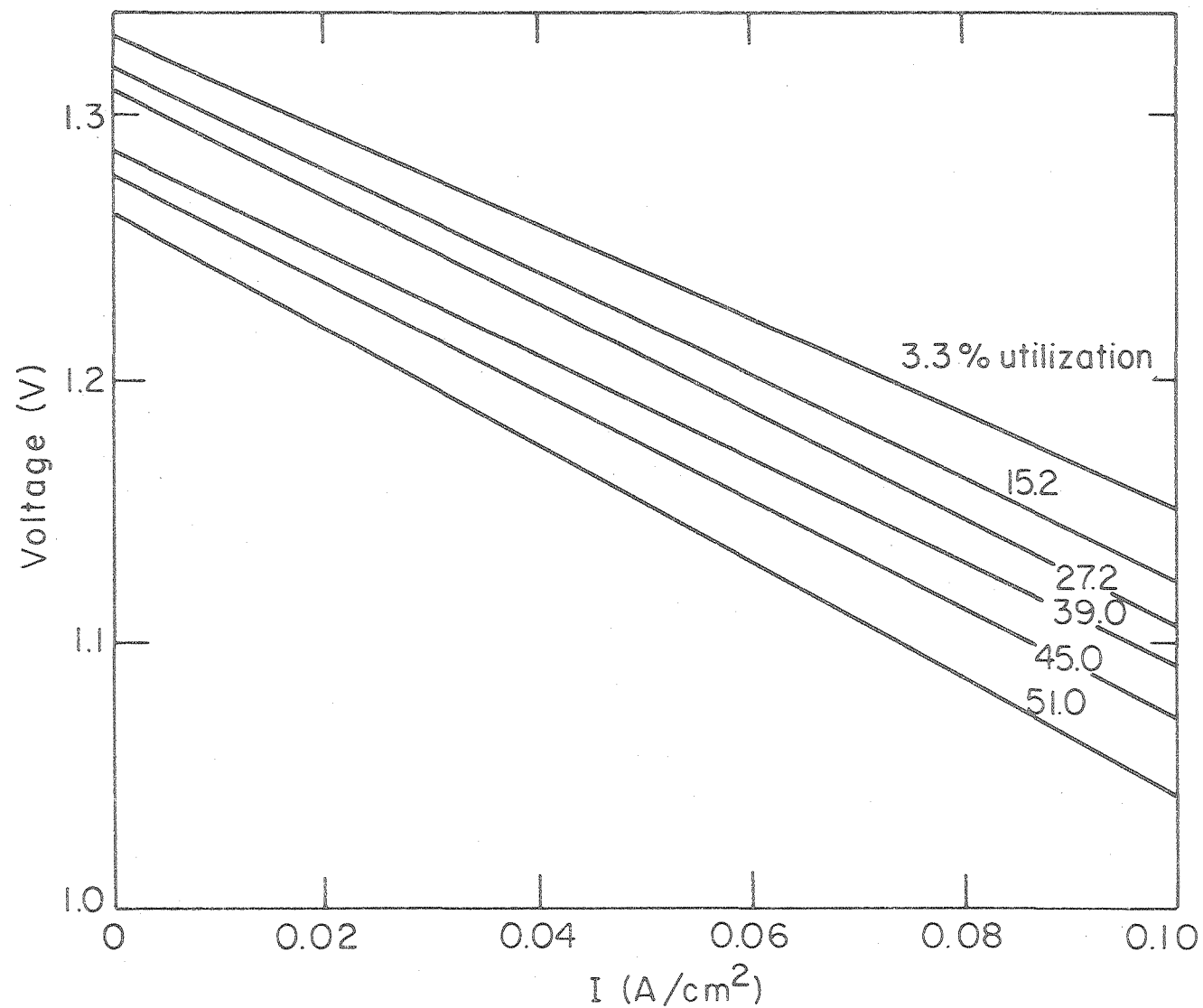
It should also be noted that a considerable quantity of lithium

can be retained in the α -Al after the β -phase has been completely utilized. For the example B in Fig. 9, the characteristics of particles at the front of the electrode when the cutoff voltage is reached are: $r_{\beta} = 0.474 \times 10^{-3}$ cm, $r_{\alpha} = 1.115 \times 10^{-3}$ cm, and $(c_{\text{Li}}^{\alpha})_o / (c_{\text{Li}}^{\alpha})_{\text{sat}} = 0.78$. This indicates that the reaction is not limited by diffusion of lithium across the α -Al and that a minimum of approximately 7.8% of the total theoretical capacity could be stored in the α -Al when no β -LiAl remains. Consequently, the available capacity in the negative electrode may be significantly lower than the theoretical estimate, and this could contribute to the apparent limitation observed in this electrode.

Polarization Characteristics

In many applications it is important to know the effect of discharge rate and depth of discharge on the useable capacity of the cell. Figure 12 shows polarization curves that represent a voltage sweep of a cell that has been discharged at a specified constant current density for a given period of time. It should be emphasized that this is not simply a cross-plot of a number of constant current discharges. Before discharge begins, there is a single current-potential curve, but the polarization characteristics will change during the discharge in a manner that depends on the total applied current. In general, polarization is greater at larger depths of discharge, and for higher current densities at a given depth of discharge.

An important feature of the curves in Fig. 12 is that they are



-41-

XBL7912-14572

Fig. 12. Effect of state of charge on theoretical cell polarization behavior. Simulation parameters as in Fig. 9, $T_o = 470^\circ\text{C}$.

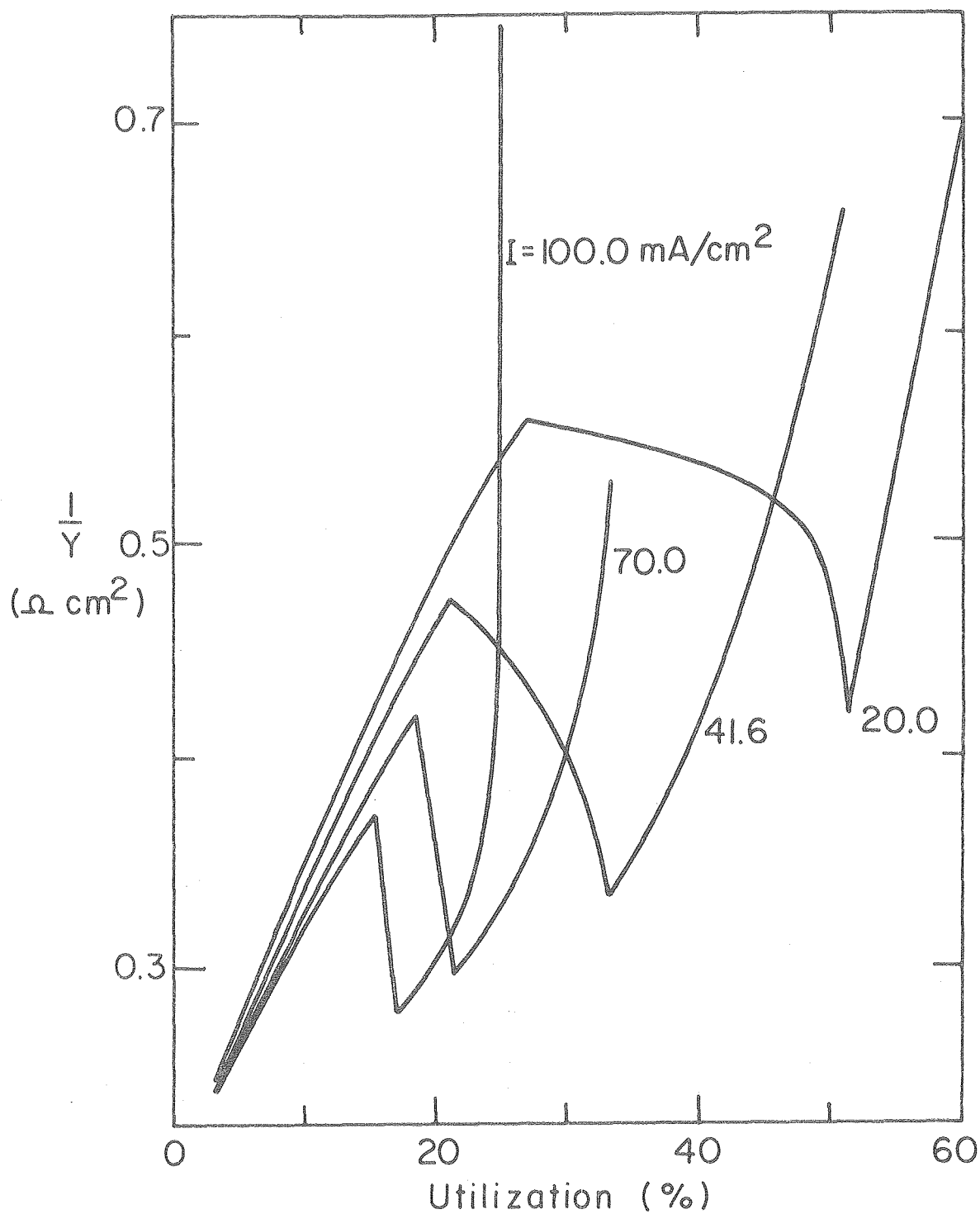
substantially straight, and there is little error in approximating them by the equation

$$I = Y(U - \Phi_+ + \Phi_-) , \quad (30)$$

where Y is the polarization conductance, given by the reciprocal of the slope of the lines, and U is the apparent open circuit cell potential, given by the ordinate intercept. In this way, the polarization characteristics of the LiAl/FeS cell can be summarized by the dependence of U and Y on the operating conditions.

Figure 13 shows the dependence of electrochemical resistance on state of charge for several different current densities. Each curve shows that, in an overall sense, the resistance increases as more active material is consumed. However, for $I = 0.1 \text{ A/cm}^2$, there is an almost discontinuous reduction in $1/Y$ at a time that corresponds to the onset of reaction IIB ($X + 2\text{Li}^+ + 2e^- \rightarrow 2\text{Li}_2\text{S} + \text{Fe}$) at the front of the positive electrode. At lower current densities the drop in resistance is neither as marked nor as abrupt, and it occurs later in the discharge (see Table 2). At each current density, the resistance rises again as porosity variations in the positive electrode lower the effective electrolyte conductivity. In practice, there is much less distinction between the intermediate reaction steps in the positive electrode. Consequently, it is not expected that the sharp changes in resistance predicted with the model, will be observed experimentally. It should also be emphasized that the model does not include the possibility for reaction of additives such as Cu_2S or CoS_2 , or for additional intermediates, such as J-phase in the conversion of FeS to Li_2S and Fe.

The dependence of the apparent open current cell potential on state



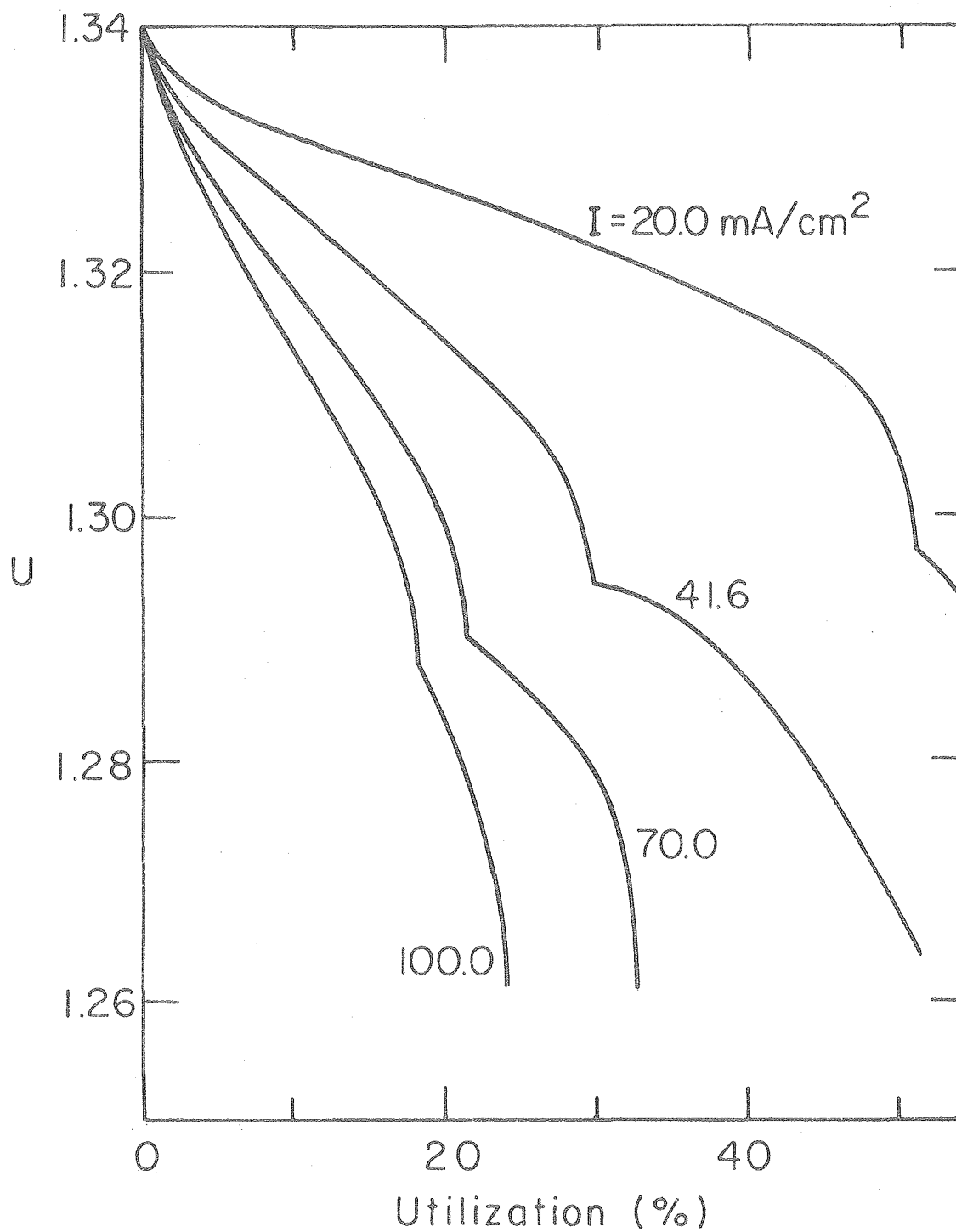
XBL7912-14573

Fig. 13. Predicted dependence of polarization resistance on utilization at different discharge rates. Parameters as in Fig. 9, $T_0 = 470^\circ\text{C}$.

of charge and discharge current density is presented in Fig. 14 and Fig. 15, for theory and experiment, respectively. In both cases, the value of U drops markedly during the discharge. The experimental results lie above the model predictions as a consequence of the presence of additives, such as Cu_2S , which raise the equilibrium open circuit cell potential. For less than about 30% utilization, the experimental curves show no systematic dependence on current density. At greater depths of discharge, U changes more markedly at higher I , as predicted in Fig. 14.

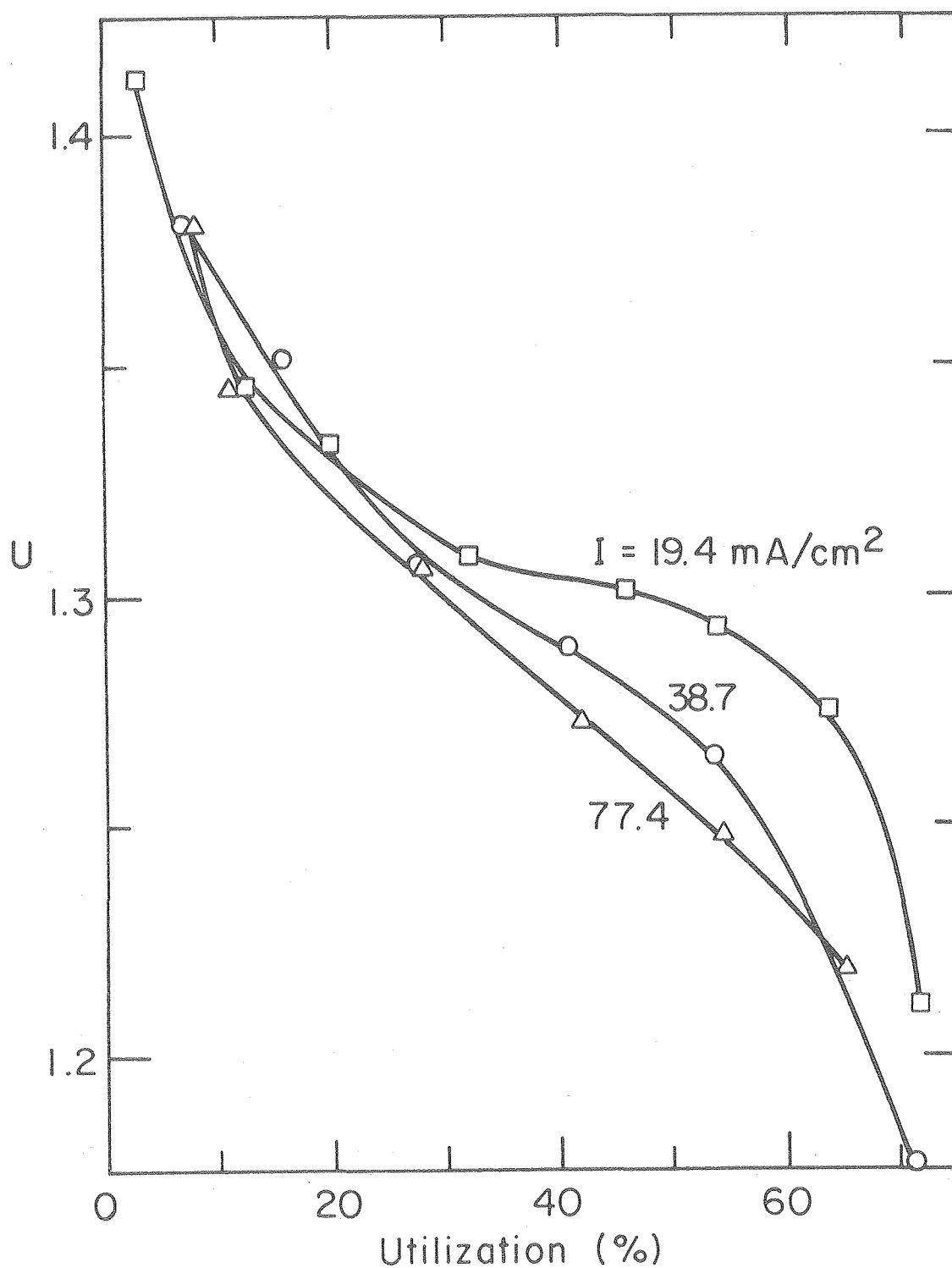
The reduction in U during the discharge can be associated with concentration polarization caused by nonuniform utilization of active material. In the negative, lithium is preferentially removed from the front of the electrode first, as illustrated in Fig. 4, and a maximum in electrolyte composition can develop part of the way through the electrode. At open circuit, the region with highest electrolyte composition becomes cathodic with respect to the rest of the electrode, and local concentration cells are set up which act in a manner that tends to reduce the composition variations. These variations can be more substantial at higher discharge rates, for a given state of change, and, consequently, the open circuit resistance can be higher in the negative electrode, leading to smaller values for U .

In the positive electrode, the situation is complicated by the possibility of simultaneous reactions. Before reaction IIB begins, $(\Phi_{+,cc})_{I=0}$ is controlled by local concentration cells that result from electrolyte composition variations, in much the same way as described



XBL 7912-14574

Fig. 14. Effect of discharge rate and state of charge on the theoretical apparent open circuit cell potential. Parameters as in Fig. 9, $T_o = 470^\circ\text{C}$.



XBL 7912-14570

Fig. 15. Variation in experimental apparent open circuit cell potential with discharge current density and utilization. Measurements taken 15 s after current investigation.²⁵

for the negative electrode. When reactions IIA and IIB both occur, a corrosion potential can be established on open circuit, which corresponds to cathodic formation of Li_2FeS_2 in the back of the electrode, and anodic formation of Li_2FeS_2 , towards the front. These reactions would be observed on current interruption, even in the absence of a composition gradient in the electrolyte. As the second reaction (IIB) progresses, the mixed corrosion potential shifts towards the equilibrium potential $U_{\text{IIB},0}$.

The positive electrode behavior is the major factor that leads to the predicted reduction in U . At higher current densities, reaction IIB begins earlier in the discharge and therefore U declines more rapidly. The less marked dependence of U on current density observed experimentally is further evidence to suggest that there is less distinction between the positive electrode reactions in practice.

Conclusions

A mathematical model has been developed that can describe the time-dependent and position-dependent behavior of a complete LiAl/LiCl , KCl/FeS cell. Composition and reaction distributions can be predicted, as well as variations in volume fractions of individual phases and electric potential within the electrodes. The results of the theoretical analysis show many of the general trends in discharge behavior that are observed experimentally. The model predicts that high internal resistance can develop in the positive electrode as a result of low local porosities which are, in turn, caused by large volume reaction

products or precipitated KCl. This implies that, with the electrode capacities currently being considered for electric vehicle applications, swelling may be a prerequisite for successful operation and thermal management of battery modules may also be important. Furthermore, an investigation of the potential distribution across the cell sandwich indicates that, before porosity reductions become critical, variations in total cell voltage are controlled more by changes in apparent open circuit cell potential than by changes in resistance across the individual electrodes.

Acknowledgment

The authors are extremely grateful to the members of the Chemical Engineering Division at the Argonne National Laboratory for many useful discussions and valuable suggestions.

This work was supported by the Division of Solar, Geothermal, Electric and Storage Systems, Office of the Assistant Secretary of Energy Technology, U. S. Department of Energy under contract No. W-7405-Eng-48.

APPENDIX

Physical Properties of the LiAl/LiCl,KCl/FeS System

Electrolyte conductivity

The dependence of bulk electrolyte conductivity on composition and temperature is described by

$$\kappa_{\infty} = (ax_A^2 + bx_A + c)e^{-E/T}, \quad (31)$$

where: $a = 18.9803$; $b = -5.0170$; $c = 9.0903$; $E = 1425.76 \text{ K}$.^{31,32} The effective conductivity in the porous medium is estimated from

$$\kappa = \epsilon \kappa_{\infty} / \zeta^2, \quad (32)$$

where the tortuosity factor ζ is directly related to porosity by

$$\zeta = \epsilon^{(1-q)/2}, \quad (33)$$

and the constant q is taken as 1.5.

Transference number

Measurements of transference numbers in binary nitrate melts show that deviations from the relation $t_i^c = x_i$ are often relatively small.³⁴ Experiments in LiCl-KCl melts³⁵ also tend to substantiate the use of this assumption which, for the molar average velocity reference frame, gives:

$$t_1^{\star} = x_A/2; t_2^{\star} = (1-x_A)/2.$$

Activity coefficient

If dissociation of electrolyte is disregarded,³⁶ the gradient of chemical potential of LiCl in the LiCl-KCl mixture can be written as

Table 3. Physical parameters used in analysis

Parameter		Value
U_o	(V)	1.34
$\partial U_o / \partial T$	(V/K)	-1.55×10^{-4}
C_p	(kJ/kg.K)	1.03
h_o	(W/m ² .K)	4.13×10^{-2}
T_A	(K)	298.15
\tilde{V}_{LiCl}	(cm ³ /mol)	20.50
\tilde{V}_{KCl}	(cm ³ /mol)	37.58
\tilde{V}_{FeS}	(cm ³ /mol)	18.55
\tilde{V}_{Fe}	(cm ³ /mol)	7.11
\tilde{V}_X	(cm ³ /mol)	46.23
σ_{Fe}	($\Omega^{-1} \text{cm}^{-1}$)	8.23×10^4
σ_{FeS}^{42}	($\Omega^{-1} \text{cm}^{-1}$)	1.90×10^3
σ_X	($\Omega^{-1} \text{cm}^{-1}$)	5.00×10^2
ρ_α	(g/cm ³)	2.70
ρ_β	(g/cm ³)	1.75
V_R^o/A	(cm)	0.03

defined by Eq. (30). The resistance R_b of a bicell can be separated into electrochemical and current collector contributions, according to:

$$R_b = \frac{1}{2A} \left(\frac{1}{Y} + R_g \right). \quad (41)$$

In the calculations, it is assumed that $R_b = 4 \text{ m}\Omega$, $Y = 1.013 \text{ }\Omega^{-1} \text{ cm}^{-2}$,²⁹ and $A = 316 \text{ cm}^2$. This yields $R_g = 1.55 \text{ }\Omega \text{ cm}^2$.

Nomenclature

a	interfacial area per unit electrode volume (cm^{-1})
a_k	relative activity of species k
A	cross-sectional area of electrode (cm^2)
c_i	concentration of species i (mol/cm^3)
\hat{C}_p	specific heat ($\text{J}/\text{g}\cdot\text{K}$)
D	diffusion coefficient (cm^2/s)
F	Faraday's constant (96487 C/equiv)
g	variable defined by Eq. (12)
h	mesh size (cm)
h_o	heat transfer coefficient ($\text{W}/\text{m}^2\cdot\text{K}$)
i_o	exchange current density (A/cm^2)
i_1	superficial current density in matrix phase (A/cm^2)
i_2	superficial current density in pore phase (A/cm^2)
i_{nj}	total current density due to reaction j (A/cm^2)
I	superficial current density to an electrode (A/cm^2)
j	$= \nabla \cdot i_2$, transfer current per unit electrode volume (A/cm^3)
j_{in}	pore wall flux of species i ($\text{mol}/\text{cm}^2\cdot\text{s}$)
L	electrode thickness (cm)
L_k	latent heat of fusion of salt k
L_T	width of cell sandwich (cm)
m	mass of cell (kg)
M_i	symbol for the chemical formula of species i
M_i	molecular weight of species i (g/mol)
n_j	number of electrons transferred in electrode reaction j

N	number of LiAl particles per unit electrode volume (cm^{-3})
\underline{N}_i	superficial flux of species i ($\text{mol}/\text{cm}^2 \cdot \text{s}$)
r_i	radius of β -LiAl in LiAl pellet (cm)
r_o	radius of LiAl pellet (cm)
R	universal gas constant ($8.3143 \text{ J/mol} \cdot \text{K}$)
R_A	parameter defined by Eq. (29)
R_g	grid resistance ($\Omega \text{ cm}^2$)
s_{ij}	stoichiometric coefficient of species i in electrode reaction j
S	parameter defined by Eq. (18)
t	time (s)
t_f	final time (s)
t_{f2}	time between start of discharge and onset of reaction IIB in positive electrode (s)
t_i^r	transference number of species i with respect to reference frame, r
T	absolute temperature (K)
T_A	temperature of surroundings (K)
T_o	initial temperature
U	apparent open circuit cell potential (V)
$U_{j,o}$	theoretical open-circuit potential for reaction j at the composition prevailing locally at the electrode surface, relative to a reference electrode of a given kind (V)
U_j^θ	standard electrode potential for reaction j (V)
U_o	open circuit cell potential (V)
\underline{v}_3	velocity of common ion in molten salt mixture (cm/s)
\underline{v}^\star	molar average velocity (cm/s)
\tilde{V}	molar volume (cm^3/mol)

\bar{V}_k	partial molar volume of salt k (cm^3/mol)
V_R	reservoir volume (cm^3)
w	reservoir width (cm)
x_k	mole fraction of salt k
Y	polarization conductance ($\Omega^{-1} \text{ cm}^{-2}$)
z_i	valence or charge number of species i

Greek Letters

α_a	transfer coefficient in anodic direction
α_c	transfer coefficient in cathodic direction
γ	mean molal activity coefficient
γ_i	exponent in Eq. (16)
γ_k	activity coefficient of salt k
ϵ	porosity or void volume fraction
ϵ_i	volume fraction of species i
ϵ_p	total volume fraction of precipitate
ϵ_{pk}	volume fraction of precipitate of salt k
ζ	tortuosity defined by Eq. (33)
η	$\Phi_1 - \Phi_2$
κ	effective solution conductivity (mho/cm)
μ_k	chemical potential of salt k (J/mol)
ν_i^k	number of ions of species i produced by dissociation of a mole of salt k
ρ	density (g/cm^3)
σ	effective matrix conductivity (mho/cm)

Φ_1	electric potential in the matrix (V)
Φ_2	electric potential in the solution (V)

Subscripts

A	salt A, e.g. lithium chloride
B	salt B, e.g. potassium chloride
cc	current collector
e	electrode
j	reaction j
k	salt A or B
lim	limiting value
o	at the electrode surface
ref	reference electrode
s	separator
sat	saturation value
α	α -Al
β	β -LiAl
+	positive electrode
-	negative electrode
∞	bulk solution property

Superscripts

A	salt A, e.g. LiCl
B	salt B, e.g. KCl
o	initial value

- α α -Al
 β β -LiAl
★ relative to molar average reference velocity

References

1. J. Newman and W. Tiedemann, AIChE Journal, 21, 25 (1975).
2. J. Newman and C. W. Tobias, J. Electrochem. Soc., 109, 1183 (1962).
3. J. S. Dunning, Dissertation, University of California, Los Angeles (1971).
4. A. Winsel, Z. Elektrochem., 66, 287 (1962).
5. W. G. Sunu, Dissertation, University of California, Los Angeles (1978).
6. W. Stein, Ph.D. thesis, Rheinisch-Westfälischen Techn. Hochschule, Aachen (1959).
7. K. Micka and I. Rousar, Electrochim. Acta, 18, 629 (1973); Ibid., 19, 499 (1974).
8. C. E. Vallet and J. Braunstein, J. Electrochem. Soc., 125, 1193 (1978).
9. K. Micka and I. Rousar, Electrochim. Acta., 21, 599 (1976).
10. W. Tiedemann, J. Newman, and F. De Sua, Power Sources, 6, 15 (1977).
11. W. Tiedemann and J. Newman, Proc. Symp. Battery Design and Optimization, S. Gross (Ed.), Princeton: The Electrochemical Society, Inc., 1979, page 23.
12. W. Tiedemann and J. Newman, Ibid., page 39.

13. P. A. Nelson et al, "High-Performance Batteries for Electric-Vehicle Propulsion and Stationary Energy Storage," Progress Report for the period 11/78-3/79, ANL 79-39, Argonne National Laboratory (May 1979).
14. R. Pollard and J. Newman, J. Electrochem. Soc., 126, 1713 (1979).
15. R. White, Dissertation, University of California, Berkeley (1977).
16. W. Tiedemann and J. Newman, J. Electrochem. Soc., 122, 1482 (1975).
17. R. Pollard, Dissertation, University of California, Berkeley (1980).
18. R. Pollard and J. Newman, unpublished work.
19. J. Newman, "Electrochemical Systems," Prentice-Hall, Englewood Cliffs, N. J. (1973).
20. R. Pollard and J. Newman, Electrochim. Acta,
21. D. Gidaspow and B. S. Baker, J. Electrochem. Soc., 120, 1005 (1973).
22. J. S. Dunning, D. N. Bennion, and J. Newman, Ibid., 118, 1251 (1971).
23. J. S. Dunning, D. N. Bennion, and J. Newman, Ibid., 120, 906 (1973).
24. H. Gu. D. N. Bennion, and J. Newman, Ibid., 123, 1364 (1976).
25. L. Redey and D. R. Vissers, personal communication.
26. D. R. Vissers, K. E. Anderson, C. K. Ho, and H. Shimotake, Proc. Symp. Battery Design and Optimization, S. Gross (Ed.), Princeton: The Electrochemical Society, Inc., 1979, page 416.
27. M. L. Saboungi and A. E. Martin, The Electrochem. Soc. Mtg., Pittsburgh, Oct. 15-20, 1978, Extended Abstract No. 339.
28. N. C. Otto and J. E. Battles in, "High Performance Batteries for Electric Vehicle Propulsion and Stationary Energy Storage," Progress Report for the period 11/78-3/79, ANL 79-39, Argonne National

Laboratory (May 1979), page 50.

29. J. Newman and R. Pollard in "High Performance Batteries for Electric-Vehicle Propulsion and Stationary Energy Storage," Progress Report for the Period 4/78-10/79, ANL 79-94, Argonne National Laboratory (November 1979).
30. C. A. Melendres, J. Electrochem. Soc., 124, 650 (1977).
31. S. V. Karpachev, A. G. Stromberg, and V. N. Podchainova, Zh. Obshchei Khim., 5, 1517 (1935).
32. E. R. van Artsdalen and I. S. Yaffe, J. Phys. Chem., 59, 118 (1955).
33. J. Newman and W. Tiedemann, "Advances in Electrochemistry and Electrochemical Engineering," Vol. 11, H. Gerischer and C. W. Tobias, Editors, Wiley-Interscience (1977).
34. J. Richter, U. Gasseling, and R. Conradt, Electrochim. Acta, 23, 1165 (1978).
35. C. T. Moynihan and R. W. Laity, J. Phys. Chem., 68, 3312 (1964).
36. M. Blander in "Molten Salt Chemistry," M. Blander, Editor, pp. 127-238, Interscience (1964).
37. E. Aukrust, B. Bjorge, H. Flood, and T. Fjørland, Annals N. Y. Acad. Sci., 79, 830 (1960).
38. B. Chu and J. J. Egan, Annals N. Y. Acad. Sci., 79, 908 (1960).
39. J. Lumsden, "Thermodynamics of Molten Salt Mixtures," Academic Press, 1966.
40. T. J. Edwards, J. Newman, and J. M. Prausnitz, Ind. Eng. Chem. Fund., 17, 264 (1978).

41. M. Hansen, "Constitution of Binary Alloys," Metallurgy and Metallurgical Engng. series, 2nd Ed., McGraw-Hill, N.Y. (1958).
42. J. P. Suchet, "Crystal Chemistry and Semiconduction in Transition Metal Binary Compounds," Academic Press (1971).

